TU Delft

Delft University of Technology

Document Version
Final published version

Licence
CC BY

Citation (APA)
Bensason, D. Y., Mulay, J. P., Sciacchitano, A., & Simao Ferreira, C. (2025). Experimental demonstration of regenerative wind farming using a high-density layout of vertical-axis wind turbines. *Wind Energy Science*, *10*(7), 1499–1528. https://doi.org/10.5194/wes-10-1499-2025

Important note
To cite this publication, please use the final published version (if applicable).
Please check the document version above.

Copyright
In case the licence states “Dutch Copyright Act (Article 25fa)”, this publication was made available Green Open Access via the TU Delft Institutional Repository pursuant to Dutch Copyright Act (Article 25fa, the Taverne amendment). This provision does not affect copyright ownership.
Unless copyright is transferred by contract or statute, it remains with the copyright holder.

Sharing and reuse
Other than for strictly personal use, it is not permitted to download, forward or distribute the text or part of it, without the consent of the author(s) and/or copyright holder(s), unless the work is under an open content license such as Creative Commons.

Takedown policy
Please contact us and provide details if you believe this document breaches copyrights.
We will remove access to the work immediately and investigate your claim.

This work is downloaded from Delft University of Technology.

Wind Energ. Sci., 10, 1499–1528, 2025
https://doi.org/10.5194/wes-10-1499-2025
© Author(s) 2025. This work is distributed under
the Creative Commons Attribution 4.0 License.

eawe european academy of wind energy
Open Access WIND ENERGY SCIENCE

Experimental demonstration of regenerative wind farming using a high-density layout of vertical-axis wind turbines

David Bensason, Jayant Mulay, Andrea Sciacchitano, and Carlos Ferreira

Flow Physics and Technology, Faculty of Aerospace Engineering,
Delft University of Technology, Delft, the Netherlands

Correspondence: David Bensason (d.y.bensason@tudelft.nl)

Received: 11 December 2024 – Discussion started: 9 January 2025
Revised: 12 March 2025 – Accepted: 14 April 2025 – Published: 30 July 2025

Abstract. The present study extends the idea of the vertical-axis wind turbine (VAWT) "vortex generator mode" for wake recovery on a wind farm scale, working towards the concept of "regenerative wind farming", where upstream turbines entrain vertical momentum for those downstream. An experimental wind tunnel demonstration of the regenerative wind farming concept for an array of nine H-type VAWTs arranged in a 3×3 grid layout is performed. Volumetric particle tracking velocimetry measures the wake within the simulated wind farm while using two vortex generator modes achieved through a fixed blade pitch. The results demonstrate the strong dependence of the wake topology of a VAWT on the streamwise vorticity system, which can be effectively modified by pitching the blades and subsequently changing the load distribution of the different quadrants of a VAWT. An increase in momentum entrainment in the wake is observed for both vortex generator modes of operation, highlighting the potential of achieving regenerative wind farming. The derived available power within the farm increases by factors of 6.4 and 2.1 for the pitch-in and pitch-out cases compared to the baseline case, respectively, considering potential rotors directly in line with those upwind.

1 Introduction

Offshore wind energy research and deployment have gained popularity in recent years, given the favourable wind resources realized by offshore turbines (Möller et al., 2012). Furthermore, the trend for both onshore and offshore wind plant projects has been to follow a cluster arrangement, given the benefits of having closely spaced rotors from economic, operational, and maintenance perspectives (Sørensen and Larsen, 2021; Shields et al., 2021). This has also become a requirement for offshore applications, given the limited space for installations that include lucrative wind resources, the possibility for bottom-fixed foundations, and limited social and political restrictions. Although the clustering of turbines has benefits on the operational side, it has been established through field, experimental, and numerical studies that densely packed turbines often experience a penalty in performance due to wake losses, leading to the underperformance of the wind plant as a whole (Barthelmie et al., 2010). The severity of these losses is strongly dependent on the layout of the farm itself and the atmospheric conditions at the respective location. Field studies of offshore farms have demonstrated losses ranging from 10 % to 23 %, depending on the turbine spacing (ranging from 4D to 12D) and wind resource (Barthelmie et al., 2007).

The wake recovery process for an isolated horizontal-axis wind turbine (HAWT) has been studied extensively, both experimentally and numerically (see reviews by Sørensen, 2011; Porté-Agel et al., 2020). In the near wake, where coherent tip and root vortices are identifiable, the entrainment of energy is ascribed to a vertical advection of momentum, accompanied by vortex leapfrogging. However, once these coherent structures break down, the process is mainly governed by turbulent kinetic energy entrainment, leading to phenomena such as wake meandering (Porté-Agel et al., 2020; Lignarolo et al., 2015). Hence, within a wind farm, the

main driver of the replenishment of momentum in the wake is governed by the rate of turbulent entrainment of kinetic energy (Stevens and Meneveau, 2017).

The greatest potential for replenishing the kinetic energy in a farm is to entrain high-momentum flow from above the rotor layer, as the turbines are often situated close to the sea surface. Given the importance of wake losses on the performance and overall efficacy of a wind plant, several strategies have been developed to mitigate them. Wake steering is a heavily researched and applied method for increasing the net performance of a wind plant through the intentional misalignment of selected turbines with the incoming flow direction, often realized through a yaw misalignment of the rotor face with the incoming wind (Fleming et al., 2017). The "steering" turbine will forfeit some performance efficiency to deflect its wake away from downstream rotors, leading to reported performance increases of the overall wind plant (Howland et al., 2019; Fleming et al., 2020). The potential gains through wake steering depend on factors such as wind resource (wind direction, speed, turbulence, etc.), turbine layout, and intrinsic baseline wake loss (Bensason et al., 2021). Like yaw control, utilizing the tilt angle to deflect the wake vertically is an extensively studied method for increasing the wake recovery rate (Kasper and Stevens, 2024; Cossu, 2021).

The underlying driver of enhanced entrainment of kinetic energy in the wake through yaw and tilt misalignment has been attributed to a counter-rotating vortex pair (CVP) generated due to the introduction of a lateral force on the wake (Bastankhah and Porté-Agel, 2016), which enhances the rate of advective flow re-energizing in the wake. This phenomenon has been further demonstrated experimentally by Bossuyt et al. (2021) for both a yawed and tilted rotor configuration, highlighting the mechanism of wake recovery using the Reynolds-averaged Navier–Stokes (RANS) equation terms. In the case of wake steering using yaw misalignment, the influx of high-momentum flow is realized from the sides of the rotor, with the wake being deflected to the side. Tilting the rotor is another wake control strategy that has been investigated and relies on the same underlying physics as the yawed case, with an included vertical force component and CVP, which entrain high-momentum flow from above and below the rotor while steering the wake upward or downward. Recent studies (Kasper and Stevens, 2024) have demonstrated the potential of this wake steering technique for large-scale wind farms. Despite the promise of these wake steering strategies, studies have commented on the impact of yaw control at a farm level on the fatigue loading of the turbines. The work by Shaler et al. (2022) concluded that, although yawing turbines in a farm that operates at and below rated conditions may not drive the ultimate loads, the fatigue loads will increase overall and become more uniform throughout the farm. Nevertheless, the relative impacts on the blade-root and shaft-bending modes are heavily dependent on the wind conditions and frequency of yaw control.

In contrast to the long wake lengths of HAWTs, vertical-axis wind turbines (VAWTs) have demonstrated an intrinsic acceleration in kinetic energy replenishment in the wake ranging up to 6D of the rotor (Wei et al., 2021). Despite their lower reported power performances, research into closely spaced, co-rotating, and counter-rotating configurations has demonstrated an order of magnitude increase in performance due to the favourable fluid interactions between the turbines (Vergaerde et al., 2020; De Tavernier et al., 2018). These findings have stimulated an increased effort towards studying the three-dimensional (3D) VAWT wakes, as they have the potential for increasing the power density of wind farms compared to the conventional HAWT arrangements (Dabiri, 2011). The wake characteristics and dynamics of VAWTs have been extensively researched through experimental and numerical investigations. Similar to HAWTs, the wake recovery process of VAWTs is characterized by the turbulent entrainment in kinetic energy from above and below the wake. However, the enhanced rate of this recovery with respect to VAWTs is mainly attributed to the presence of dominant streamwise vortical structures shed by the blade tips throughout the periodic cycle of the rotor (Huang et al., 2023b), which entrain momentum through an advective process. Numerical simulations by Boudreau and Dumas (2017) demonstrated the persistence of these advective contributions towards wake replenishment in the wake for a cross-flow turbine compared to an axial turbine.

A recent study by Huang et al. (2023b) experimentally demonstrated the relationship between the VAWT load distribution and trailing vorticity structures. By simplifying the load distribution to an idealized actuator cylinder surface (Madsen et al., 2014), they linked the deformation and deflection of the VAWT wake topology to the distribution of load discretized between the different quadrants of the rotor cycle. By redistributing the load among the upwind, downwind, windward, and leeward quadrants, the strength of the trailing vortical structures shed in the respective quadrants can be increased or decreased, leading to modification of the wake topology. This concept was further developed and confirmed via numerical simulations (De Tavernier et al., 2020; De Tavernier and Ferreira, 2019). An effective method to modify the load cycle of a VAWT is through blade pitch. Experimental results by LeBlanc and Ferreira (2022b) demonstrated the impact of cyclic and fixed blade pitch motions on the normal load and subsequent thrust vectoring of an H-type VAWT, confirming the augmentation and redistribution of load among the different quadrants of the cycle. Subsequent planar flow-field measurements at the mid-span of the rotor blade at different phases confirmed the normal load distribution with varying pitching schemes (LeBlanc and Ferreira, 2022a). The work of Huang et al. (2023b, a) measured the wake of an H-type VAWT using a stereoscopic measurement system at discrete downwind planes ranging up to 10D with different fixed pitch offsets applied to the blades, namely, a case where blades are pitched inward (inside the rotor swept

volume) and outward. A comprehensive visualization of the wake deformation and deflection as a function of the augmented trailing vorticity was revealed, demonstrating significant gains in available power for potential downstream rotors of up to 150 % at $5D$. An enhanced advective momentum flux above and below the rotor was observed for the case where the load is shifted towards the upwind half of the blade cycle. In contrast, the lateral advective kinetic energy entrainment is increased when the load is shifted towards the downward half.

Current experimental studies, which are 2D2C or 2D3C, provide limited information on the three-dimensionality of a VAWT wake topology and vortex strength due to the intrinsic limitations of planar measurements. This is further magnified by the use of blade pitching schemes, which rely mainly on the modification of these vortical structures, leading to heavy 3D wake phenomena (De Tavernier et al., 2020). The literature on experimental 3D-resolved wakes of VAWTs in wind tunnel settings is limited (Brownstein et al., 2019; Caridi et al., 2016; Ryan et al., 2016; van der Hoek et al., 2024) and is lacking for rotors using the aforementioned wake control strategy. Further, an experimental demonstration with a 3D-resolved flow field of the potential of blade pitch towards wake re-energization in a farm setting has not been investigated to date. The work of Brownstein et al. (2019) yielded 3D flow-field measurements for a set of two turbines in close proximity to highlight the benefits of high-density VAWT arrangements but was limited to a wake measurement domain up to 3D.

The goal of this paper is to report the 3D-resolved wake measurement results of a wind-tunnel-scaled high-energy-density wind farm made of VAWTs with and without wake control strategies in a standard grid arrangement. Although staggered as opposed to in-line arrangements have been shown to be superior for optimum farm performance (Hezaveh and Bou-Zeid, 2018a; Hezaveh et al., 2018b), the objective of this work is to highlight the efficacy of the passive blade pitch recovery strategy for the most detrimental conditions for wake losses. The results from this study provide a basis for ongoing and future numerical model validation. The flow fields at the inflow, within, and at the outflow of the farm are measured using 3D Lagrangian particle tracking, focusing on the central column of the farm. This work offers a detailed analysis of the vortical structures in the wind farm and how the wake topology changes when these structures are enhanced. An overview of the working principle of the "vortex generator" mode of VAWTs and its application towards regenerative wind farming is provided in Sect. 2. The 3D wake measurement technique and wind tunnel simulated wind farm setup are described in Sect. 3. The discussion of the results given in Sect. 4 focuses on the modification of the trailing vorticity system and the subsequent impact on the wake topology. The wake recovery is quantified, and the driving mechanisms for recovery are isolated via an energy budget analysis.

2 Working principle of the vortex-generator mode

The working principle of an H-Type VAWT as a vortex generator has been numerically and experimentally explored by Huang et al. (2023b, a), in which the link between the wake topology and deflection to the quadrant discretized blade load distribution is evaluated.

The working principle can be best described by simplifying the phase-dependent VAWT blade load as an idealized actuator cylinder (AC) that includes radially dependent normal loads, which represent the blade integrated loads (Madsen et al., 2014), as visualized in Fig. 1. The AC simulated normal loading and wake characteristics for VAWTs have been validated using high-fidelity models and experimental results by De Tavernier et al. (2020), De Tavernier and Ferreira (2019), and Martinez-Ojeda et al. (2021). The work of Huang et al. (2023b) demonstrated that a modification in the idealized load distribution of the AC could lead to enhanced wake deformation and deflection depending on the load distribution between the different quadrants. The load profile of the AC can be modified in several ways, including pitching the struts connecting the blades to the tower (Mendoza and Goude, 2019; Ribeiro et al., 2024), inclining the angle of the rotor blade (Guo and Lei, 2020), and applying blade pitch (LeBlanc and Ferreira, 2022b). The present work uses the blade pitch method for modifying the idealized AC load. As a proof of concept for using this vortex generator mode for a wind tunnel simulated wind farm, fixed-pitch offsets are used (constantly applied throughout the entire rotor cycle), as in the work of Huang et al. (2023b).

A top-view schematic representation of the idealized actuator cylinder load for the vortex generator cases is shown in Fig. 1, adapted from the work of Huang et al. (2023b), for a rotor rotating anti-clockwise. Three cases are shown: the baseline, where no fixed pitch is applied; the pitch-in case, where the blade is pitched towards the supporting tower; and the pitch-out case, where the blade is pitched away from the rotor volume. The VAWT cycle is discretized into four quadrants, namely, upwind windward (UW), upwind leeward (UL), downwind leeward (DL), and downwind windward (DW). The actuator circumference (corresponding to the upper blade-tip trajectory) is colour-coded based on the direction of the trailing tip-vortex shed from each quadrant in the inertial frame of reference, with red and blue as anti-clockwise and clockwise, respectively. This cyclic variation in tip-vortex direction is intrinsic to VAWT aerodynamics and is a product of the variation in relative angle of attack and, subsequently, the direction of circulation of the blade-tip vortex (Tescione et al., 2014; Bensason et al., 2023). The normal arrows represent the blade-integrated loads. Below each mode, the projected frontal area of the top half of the rotor ($z/D > 0$) (green-shaded region) at a generic downstream plane is shown with the projected intersections of the quadrant-labelled trailing vortical structures. The directions of rotation of these structures are indicated by arrows em-

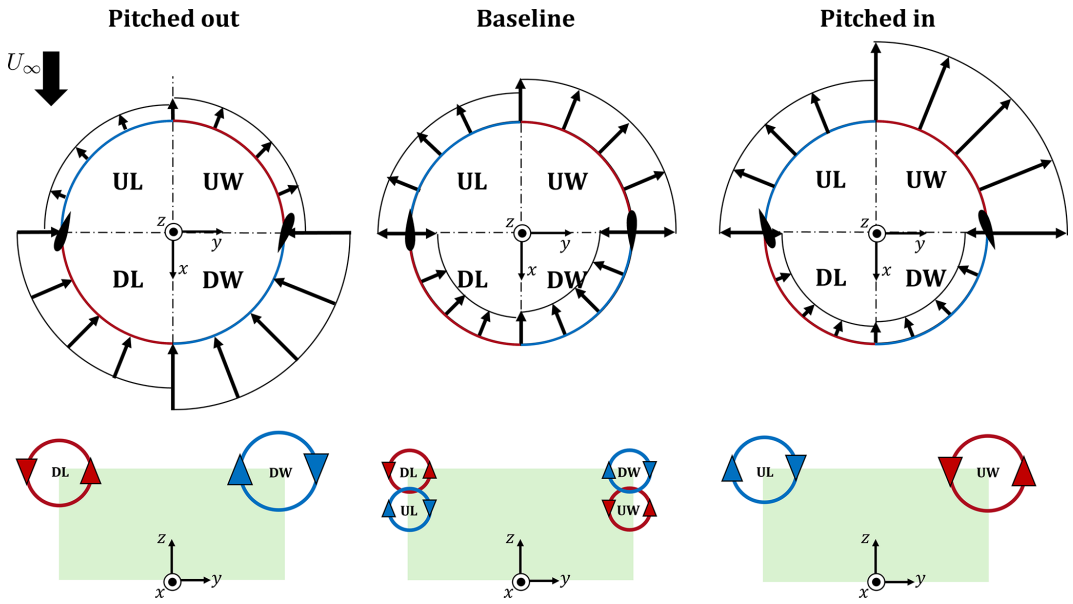

Figure 1. Top-view schematic of the simplified AC force fields for the three "vortex generator" modes of operations adapted from Huang et al. (2023b) and Bensason et al. (2024), namely, the baseline case (where no pitch is applied), a pitched-in case, and a pitched-out case. Blades at a phase position of $\theta = 0°$ are shown at exaggerated sizes and pitch angles to demonstrate the pitching convention. The coordinate systems are shown at the centre of the AC, and the rotation direction is anti-clockwise. The quadrants of the idealized AC are labelled as upwind windward (UW) $0° < \theta < 90°$, upwind leeward (UL) $90° < \theta < 180°$, downwind leeward (DL) $180° < \theta < 270°$, and downwind windward (DW) $270° < \theta < 360°$. The top edges of the rotor cylinder are colour-coded based on the direction of rotation in the internal frame of reference of the trailing blade-tip vortices, with red and blue as anti-clockwise and clockwise, respectively. The top half of the rotor's projected frontal area (green) at a generic measurement plane downstream is shown below each mode. The projected dominant quadrant-labelled streamwise vortical structures stemming from the blade tips for each pitch case are shown via circular arrows.

bedded in the idealized circular vortex intersection. As the inflow is uniformly laminar and no ground effect is included in this study, the wake topology should be symmetric about the symmetry plane $z/D = 0$. Hence, the vortical structures stemming from the bottom blade tips will be equal and opposite to those generated at the top, in accordance with the Helmholtz theorem.

The AC loads shown for a VAWT are simplified to understand the trailing vorticity and subsequent wake topology described in the results that will follow. In reality, the blade load results from both the normal and tangential loads, of which the normal is dominant, which varies azimuthally throughout the cycle (LeBlanc and Ferreira, 2022b). Furthermore, under the realistic operating conditions of a VAWT, where unsteady effects are present, such as dynamic stall, turbulence, and dynamic inflow, the load profiles can change significantly. Experimentally acquired blade load profiles as a function of azimuth with variable pitch control are presented by LeBlanc and Ferreira (2022b) for a straight-bladed VAWT and highlight this non-uniformity. Nonetheless, these schematics are sufficient for describing the impacts of AC load modification on the wake, with each case described as follows.

Baseline case. In the case where no pitch is applied, the AC loading is intrinsically asymmetric. The upwind half of the cycle will experience a higher load than the downwind half, as the latter involves the blades operating in their own wake (LeBlanc and Ferreira, 2022a; De Tavernier et al., 2020). Furthermore, the windward passage of the blade will exhibit larger loads than the leeward due to the higher relative wind speed as the blade moves into the wind. Despite the more favourable load of the upwind quadrants, the trailing vorticity in the near wake of the rotor will exhibit the counter-rotating vortex pairs (CVPs) from both halves of the cycle (Huang et al., 2023b; Bensason et al., 2023; Tescione et al., 2014). The aforementioned favourable loading on the windward passage on the blade leads to an intrinsic asymmetry in the wake in favour of the windward side, as shown experimentally by Tescione et al. (2014) and Bensason et al. (2024).

Pitched-in case. When the blades are pitched inward, the load is shifted towards the upwind half, as shown by the increased integrated load magnitude along the upwind quadrants. As a result, the vortical structures generated in the upwind half are energized and become the dominant CVP in the wake, as shown in the projected frontal area, with the less-energized pairs stemming from the downwind half changing in direction and merging with the dominant pair, as experimentally demonstrated through phase-locked wake measurements of the near wake of a VAWT by Bensason et al. (2024). Once again, the windward side is more energized than the

leeward, leading to a stronger UW than the UL vortex, visualized by the difference in vortex size. The impact of this load modification is 2-fold. Firstly, the domain CVP on the upper tips will induce a significant axial downwash in the wake, with high-momentum flow from above the rotor being injected into the volume while low-momentum wake is ejected out laterally. Secondly, given the imbalance in load between the windward and leeward halves of the rotor, a strong lateral force will be imposed on the wake, leading to a lateral deflection of the low-momentum flow towards the windward side. The results of Huang et al. (2023b) have confirmed this mode of operation, highlighting the potential of the enhanced advective momentum transfer between the freestream and wake towards an accelerated wake recovery.

Pitched-out case. Finally, when the blade is pitched out, the AC load is shifted towards the downwind half of the cycle. Hence, the rotation directions of the vortical structures shed from the blade tips will be opposite those for the positive pitch case. As in the aforementioned mode of operation, the dominant vortical structures in the wake will lead to a modification in topology, with an induced upwash and downwash in the upper and lower halves, respectively, while high-speed momentum is injected from the sides of the rotor. Meanwhile, the load imbalance between the leeward and windward sides results in a lateral deflection of the wake centre towards the leeward side. This mode of operation was also experimentally demonstrated by Huang et al. (2023b); however, it showed to have less potential than the pitched-in mode of operation with respect to streamwise momentum recovery, presumably due to the intrinsically lower efficiency in the downwind half of the cycle, as discussed for the baseline case.

A schematic representation of an array of three uniformly spaced inline VAWTs is shown in Fig. 2 for the three modes of operation. The wake structures at the midplane $y/D = 0$ are represented by grey-shaded areas, with the streamwise velocity profiles at different downstream locations $U_x(x)$ represented by arrows of varying size (magnitude). For this study, the inflow is uniform laminar with speed U_∞ without a ground effect. Hence, the wake structure and re-energization mechanism will be symmetric about the xy symmetry plane. Additionally, arrows representing advective and turbulent entrainment of kinetic energy in the wake are represented by purple and blue arrows, respectively. The sizes of these arrows reflect the relative magnitude of the contributions in the wake.

For the baseline case, in the near wake, the wake re-energization is mainly caused by the lateral momentum advection due to the cohesive vortical structures shed in the wake, as included in Fig. 1 (Boudreau and Dumas, 2017). As the structures diffuse and mix, the wake recovery process will transition towards a turbulent kinetic energy entrainment. With no strong lateral force induced by the rotor load, the wakes of different turbines will continue to superimpose on each other within the farm, growing in size due to the wake expansion.

For the negative pitch case, the advective contribution towards the wake recovery will significantly increase due to the dominant vortical structures highlighted in Fig. 1. Given the direction of rotation of the downwind tip-vortex structures, high-momentum flow will be injected in the wake from the lateral direction, while the low-momentum wake is ejected out above and below the rotor. Hence, the wake will recover more compared to the baseline case, as highlighted by the non-grey-shaded regions downstream of the rotor. Meanwhile, the region of flow deficit will grow above and below the rotor compared to the baseline case.

Finally, for the positive pitch case, the streamwise vortical structures will inject high-momentum flow from above and below the rotor while ejecting the low-momentum flow laterally outward. Hence, the wake will contract in the axial direction, increasing the availability of high-energy streamwise flow for downstream rotors.

3 Experimental methods

3.1 Wind tunnel

The experiments are conducted in the Open Jet Facility (OJF) of TU Delft's Faculty of Aerospace Engineering, visualized in Fig. 3. The tunnel has been used for wake studies of the same VAWT geometry in a single and two-turbine array (Huang et al., 2023c, b) as well as for other scaled VAWT experiments (Tescione et al., 2014; LeBlanc and Ferreira, 2022a). The closed-loop wind tunnel has an octagonal outlet of dimension 2.85 m × 2.85 m with a contraction ratio of 3 : 1. The jet stream bound shear layer angle and turbulence intensity are reported as 4.7° and 0.5 %, respectively (Lignarolo et al., 2014). The region of uniform flow extends 6 m beyond the tunnel exit, which encompasses the measurement volume for this experiment.

3.2 Wind turbine model

The H-type Darrieus VAWT model is designed in-house and is an altered version of the geometry used by Huang et al. (2023b). A detailed schematic is provided in Fig. 4 and illustrated in a wind farm array in Fig. 3. The rotor geometry is mounted on a rotor shaft with a 10 mm diameter and 1100 mm height, which runs through a tower. The rotor tower is 700 mm tall, is made of milled aluminium, and follows a tapered profile with base and tip diameters of 50 and 25 mm, respectively. Further, the tower houses roller bearings at the top and bottom to minimize any deflections of the shaft resulting from imbalances in the rotor. The tower is fastened to an aluminium stand, which connects to an in-house-designed three-component balance. The stand houses a Maxon EC 90 260 W DC motor, which is controlled via an ESCON 50/5 controller that rotates the rotor shaft at a

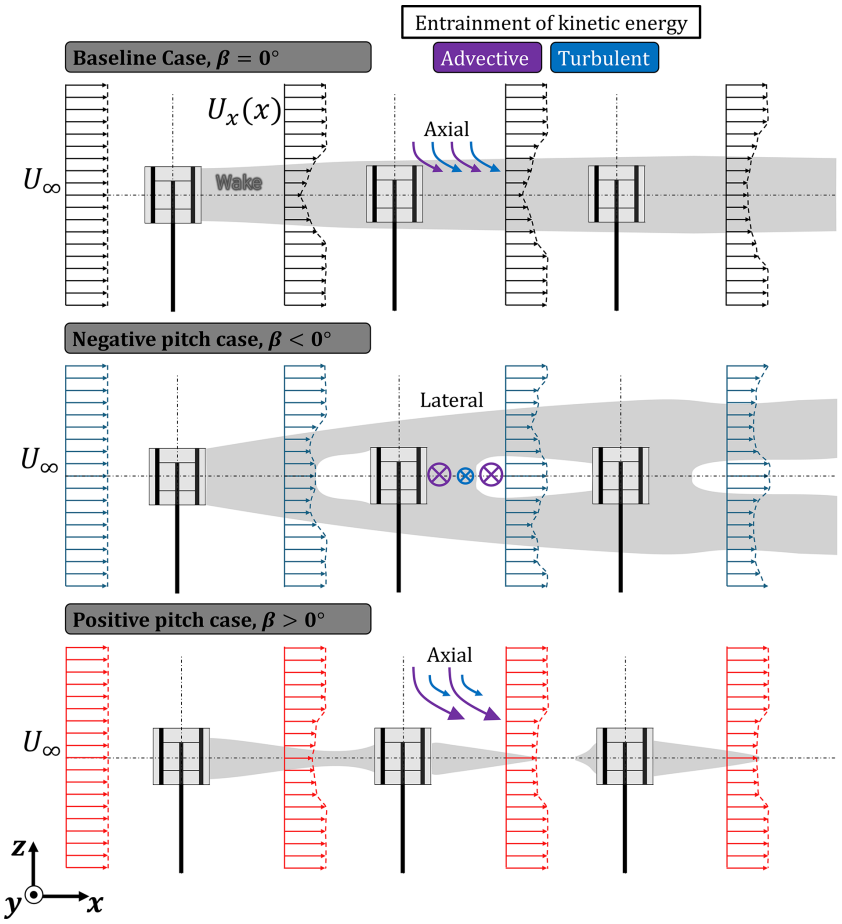

Figure 2. Schematic representation of the wake evolution at the xz plane ($y/D = 0$) of an array of three uniformly spaced inline VAWTs with laminar-uniform inflow U_∞. The illustration is a simplified adaptation of numerical results obtained by Huang (2023b). The grey-shaded region represents simplified wakes, while the white areas show the freestream flow. The profiles of the streamwise velocity $U_x(x)$ within the array for the three pitch cases β are shown in black, blue, and red for the baseline, pitched-out, and pitched-in cases, respectively. As no ground effect is included in this study, the wake structure and re-energization process will be symmetric about the xy symmetry plane. The advective and turbulent contributions towards the wake recovery for the three modes of operation are portrayed using purple and blue arrows, respectively. The size of the arrows corresponds to the relative contributions of each for the three cases, with the direction labelled above. In this case, the axial corresponds to the directions above and below the rotor (z axis) and lateral from the sides of the rotor (y axis).

constant rpm in either the clockwise or anti-clockwise direction. Prior to the wind farm flow-field measurements, the cycle-averaged streamwise and lateral thrust components of the rotor are measured at different tip-speed ratios using the force balance. The force balance has a maximum range of ± 50 N and a maximum error of $\leq 0.1\,\%$. Further details of the design are provided by Huang et al. (2023b).

The rotor geometry consists of two straight untapered blades with a span of $S = 300$ mm fastened to the rotor shaft via two struts separated by 150 mm, as shown in Fig. 4. The struts have an oval-shaped profile with a span, thickness, and chord of 300, 4, and 30 mm, respectively. The blades are made of extruded aluminium with a NACA0012 profile with a chord $c = 30$ mm. The different fixed-pitch adjustments are realized by interchanging modular 3D-printed adapters between the blade and strut at all four connection points, shown in blue in Sect. 3.2. The adapters have the same chord and thickness as the struts. In this experiment, the fixed-pitch settings of $\beta = -10$, 0, and 10° about the mid-chord are used to allow for a qualitative comparison with the work of Huang et al. (2023b, c). Positive and negative pitch are defined as pitch inward towards the tower and outward, respectively. The rotor diameter is $D = 300$ mm. All components of the rotor are painted black to minimize the reflections during the flow measurement process, as described in Sect. 3.3. The rotor solidity is $\sigma = NcS/A = 0.2$, where $N = 2$ is the number of blades and $A = 0.09\,\mathrm{m}^2$ is the projected frontal area of the rotor. The wind tunnel blockage of a single rotor is 0.011, considering the projected frontal area of the rotor.

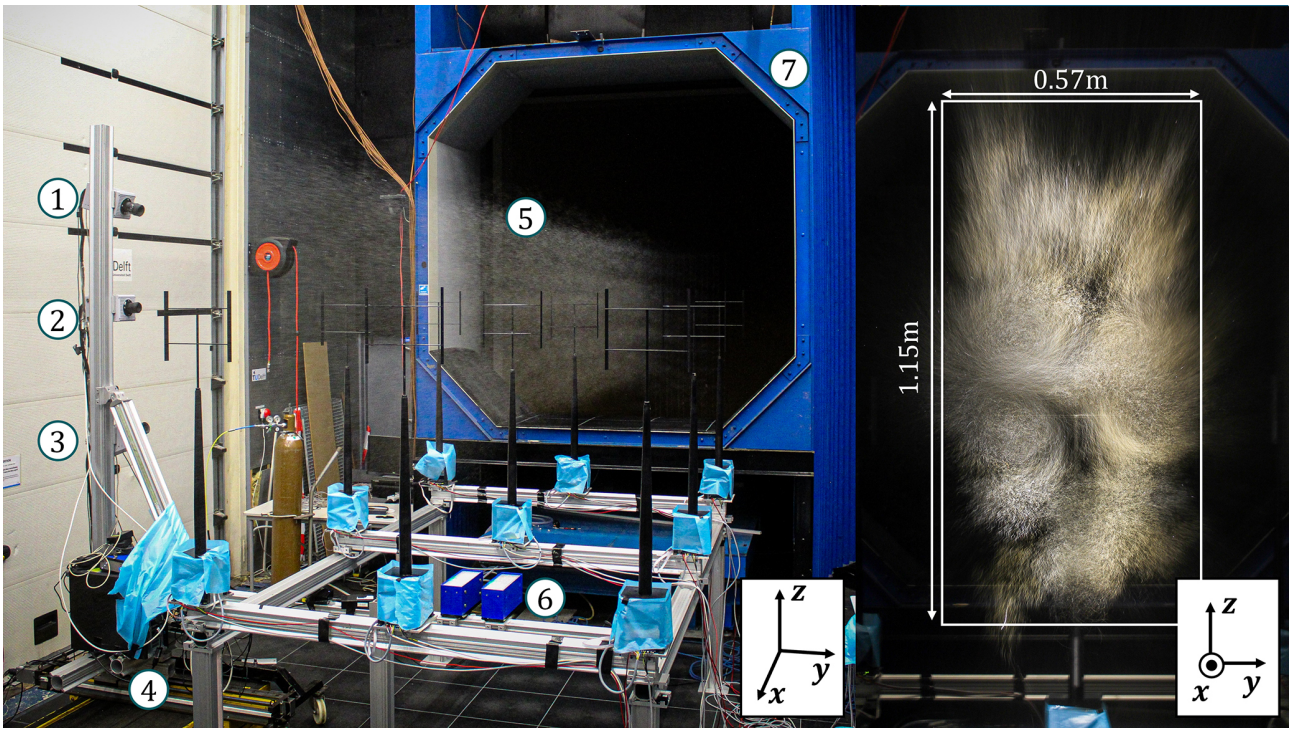

Figure 3. Experimental setup in the OJF. On the left, the main components are labelled and defined as follows: (1) camera 1, (2) camera 2, (3) camera 3, (4) traversing system, (5) helium-filled soap bubble (HFSB) stream tube, (6) LEDs, (7) OJF outlet. On the right, a close-up image of an illuminated measurement volume with the dimensions of the field of view is marked, showing the deformed stream tube of the HFSBs. The coordinate systems for the two panels are shown on the bottom right.

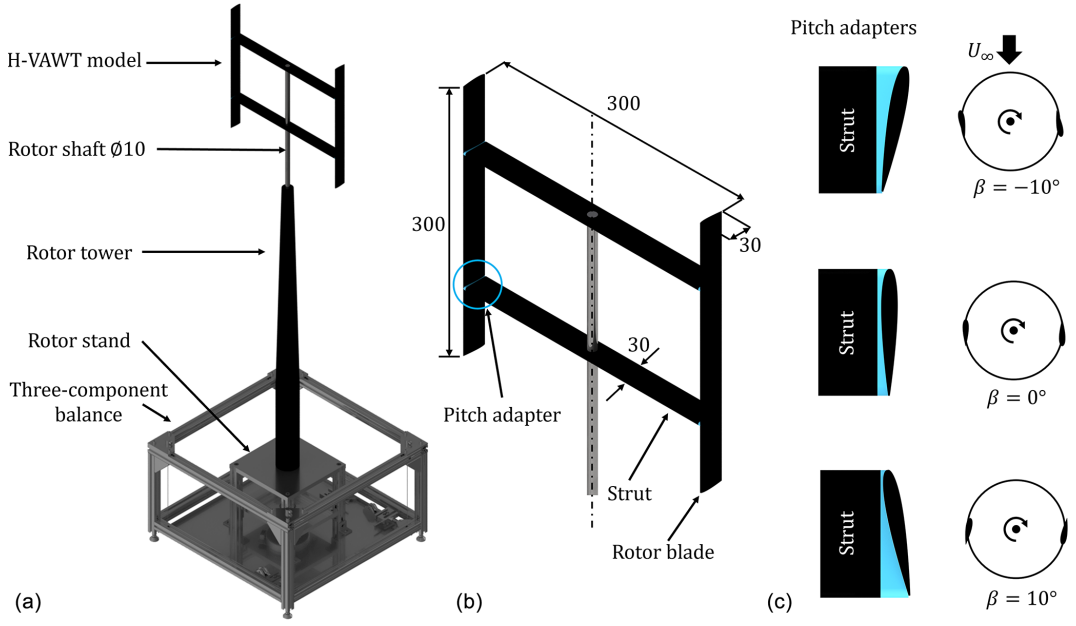

Figure 4. **(a)** Rendered schematic of the H-type VAWT model mounted on the three-component balance, and **(b)** rendering of the rotor geometry. The turquoise circle outlines one of the four pitch adapters situated at the connection point between the blades and struts. **(c)** Top-view rendering of the three pitch adapters (turquoise) mounted between the blade and struts, with a pitch towards and away from the tower denoted as positive and negative pitch, respectively. The top-view schematic of the rotor shows exaggerated blade sizes for clarity. The main components of the rotor are labelled, with all dimensions in mm.

3.3 Flow measurement system

The velocity fields are obtained through 3D Lagrangian particle tracking. Seeding is generated using a rake placed in the settling chamber of the OJF made up of 200 nozzles, each releasing neutrally buoyant helium-filled soap bubbles (HFSBs) at a rate of $30\,000\,\mathrm{s}^{-1}$ and an average diameter of 0.4 mm (Faleiros et al., 2019). Given the rake dimensions and the contraction ratio of the outlet, the seeded stream tube is approximately $0.57\,\mathrm{m} \times 1.2\,\mathrm{m}$, as visualized in Fig. 3. The resulting seeding concentration is on average 1 HFSB cm^{-3} (Caridi et al., 2016). The rake has been shown to minimally impact the turbulence intensity of the incoming flow by 0.8 % (Giaquinta, 2018). Given the limited size of the generated stream tube and desired lateral measurement volume, the seeding rake is translated along the width of the tunnel to adequately seed the desired measurement volume, as described in Sect. 3.4.

The flow tracers are illuminated from below the farm using the LaVision LED-Flashlight 300, as shown in Fig. 3, with a pulse length of 200 µs. Images of the illuminated bubbles are recorded using three Photron FASTCAM SA1.1 high-speed cameras (CMOS, 12 bit, 20 µmm pixel pitch). Image frames are acquired at a frequency of 500 Hz with an image resolution of $1024\,\mathrm{px} \times 1024\,\mathrm{px}$. Cameras 1, 2, and 3 have mounted lenses of 60, 50, and 60 mm focal length, respectively, with a set numerical aperture of $f/22$. An individual measurement volume is approximately $0.17\,\mathrm{m}^3$, resulting in a digital image resolution of $1.6\,\mathrm{px\,mm}^{-1}$ with a magnification factor of $M = 0.03$. A total of 4600 frames are captured per measurement volume, corresponding to an acquisition time of 9.2 s. Given the rotational frequency of the rotor during the wake measurements of $\omega = 70\,\mathrm{rad\,s}^{-1}$, approximately 102 rotor revolutions are captured. The illumination and imaging are synchronized using a LaVision PTU-X timing device. The cameras and LEDs are mounted rigidly on a traversing bed, visualized in Fig. 3. This allows for the translation of the measurement volume in the streamwise and lateral directions such that several can be stitched together without the need for re-calibrating the acquisition system, as described in Sect. 3.4.

The acquired frames are processed using the LaVision DaVis 10 software. First, background removal is applied by subtracting a minimum time filter with a kernel of five images. Geometric calibration of the camera positions relative to the measurement domain is performed using a calibration plate, followed by a volume self-calibration using an unperturbed flow-field recording of particles (Wieneke, 2008). The residual measurement errors fall below 0.1 pixels for all three cameras. Next, tracer trajectories are evaluated using the Shake-the-Box (STB) algorithm (Schanz et al., 2016). The number of identified particle tracks per time step ranges between 8000 and 15 000, depending on the specific measurement volumes in the farm and pitch case, due to the strong deflection of tracers in and out of the field of view. Next, the individual STB volumes measured within the overall farm measurement volume shown in Fig. 5 are stitched together with the corresponding lateral and streamwise offsets recorded using the traversing system, as described above, yielding a total measurement volume of approximately $5.3\,\mathrm{m}^3$. Finally, the binning step involves mapping particle tracks of the fully stitched volume on a Cartesian grid by spatially averaging over smaller cells (Agüera et al., 2016). In this study, all time stamps are binned together to yield a time-averaged wake measurement. The sub-volume size is $128 \times 128 \times 128$ voxels, where one voxel = 80 mm. Given an overlap of 75 %, the final grid spacing of the velocity vectors is 19.9 mm. A justification of the selected sub-volume size is provided in Appendix A, demonstrating its adequacy for capturing the wake-scale dynamics in the wind farm.

3.4 Case overview

The freestream wind speed is constant at $U_\infty = 3\,\mathrm{m\,s}^{-1}$. The rotational frequency of all of the rotors is maintained at $\omega = 70\,\mathrm{rad\,s}^{-1}$, equating to a tip-speed ratio of $\lambda = \omega R/U_\infty = 3.5$ and diameter-based Reynolds number of $Re_\mathrm{D} = 6.1 \times 10^4$. Previous works have studied the wakes of VAWTs at similar Reynolds numbers (Bachant and Wosnik, 2016; Rolin and Porté-Agel, 2018; Huang et al., 2023b), concluding that the wake topology is largely Reynolds-insensitive. This corroborates the conclusions drawn by Wei et al. (2021), who observed similar wake characteristics between a full-scale VAWT at in situ conditions and water-channel measurements at a Reynolds number 2 orders of magnitude lower.

A series of nine identical turbines are arranged in a grid beyond the exit of the OJF, as shown in Fig. 3 and the top-view schematic in Fig. 5. The streamwise and lateral spacing between the rows and columns is $5D$ (1.5 m) and $3.18D$ (0.953 m), respectively. The resulting gap between the blades of the peripheral rotors and the projected edge of the outlet is $1.1D$. The shear layer of the open jet is reported to increase the turbulence intensity to up to 10 % at approximately $0.3D$ from the outlet edge (Lignarolo et al., 2014). Hence, particularly for the positively pitched case, the wakes of the peripheral columns may interact with the shear layer of the jet. While this is a limitation of the experimental facility, the impacts on the wake topology of the central column will be investigated through ongoing numerical validations, as discussed in Sect. 5. All rotors operate at the same rotational frequency in the clockwise direction with respect to the incoming flow. The phases of the rotors are not synchronized. The origin of the coordinate system $x = y = z = 0$ is defined as the geometric centre of the first rotor in the central column. Note that, for the results discussed in Sect. 4, the measured wakes have been mirrored along the y axis (as if the rotors rotate anti-clockwise) for consistency with previous works by Bensason et al. (2023, 2024).

Table 1. Overview of the wake recovery strategy test cases.

Pitch case	Description
$\beta = -10°$	The blades of all of the rotors are pitched out.
$\beta = 0°$	No fixed pitch is applied to the rotors (baseline).
$\beta = 10°$	The blades of all of the rotors are pitched in.

The three modes of operation described in Sect. 2 are used for this experiment. To allow for a qualitative comparison with these previous works by Huang et al. (2023b), the same fixed-pitch settings of $\beta = -10$, 0, 10° are used. The sign convention is highlighted in Fig. 4. The case with no wake mixing strategy $\beta = 0°$ will be referred to as the baseline case. The wind farm wake is measured for these three pitch cases independently, where all rotors are pitched by the same amount. Furthermore, the grid spacing between the rotors is kept constant, with no lateral offset spacing between the rotors applied. A description of these three cases is provided in Table 1.

As discussed in Sect. 3.3, the full-time-averaged wake of the wind farm is measured by stitching several smaller measurement sub-volumes together using the traversing bed, which has an accuracy of ±0.01 mm. An example of the boundaries and an instantaneous tracked HFSB single-measurement sub-volume within the farm domain is shown in Fig. 5. The overall measurement extent of the volumes at different positions within the farm for the $\beta = 10°$ case is shown in Fig. 5 via coloured lines. The size of the measurement volumes varies between the different farm positions due to the strong wake deflections experienced for the vortex generator mode cases, leading to frequent areas in the flow void of any HFSB, as shown in Fig. 3. To account for this, several measurement sub-volumes are captured, accompanied by frequent movement of the seeding rake in the settling chamber, and rigid camera and LED construction are used to distribute tracers more evenly and capture the full wake. The coloured lines delineate the overall measurement volume once the individual sub-volumes are stitched together, as discussed in Sect. 3.3. In the inflow of the farm, two sub-volumes are measured. Between the first and second rows, nine sub-volumes are measured. Between the second and third rows, 15 sub-volumes are measured. Finally, in the outflow of the farm, 12 sub-volumes are measured. Note that, due to the optical obstructions of the rotors and the nature of the measurement system, the volumes inline with the rotors are omitted from the analysis in Sect. 4. The individual sub-volumes are translated such that there is sufficient overlap between them within a given domain – these range between $0.7D$ and $1.6D$ in the streamwise direction and $0.3D$ and $1D$ in the lateral direction. The final measurement domain encompasses a total streamwise distance of $17.6D$, extending $2D$ and $5.6D$ in the inflow of the farm and the wake behind the farm, respectively. The lateral measurement ranges vary

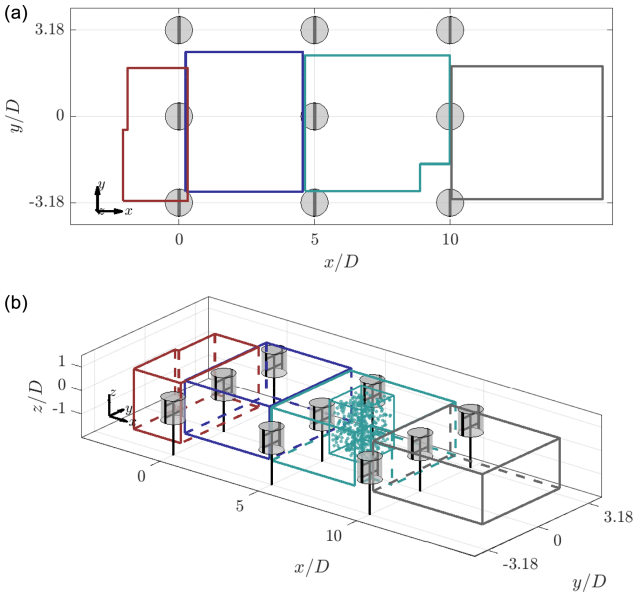

Figure 5. Top-view **(a)** and isometric-view **(b)** schematic of the wind farm arrangement. The wind turbines are shown at phase-locked positions $\theta = 0°$, with the surrounding grey-shaded cylinders denoting the idealized AC surfaces. The grid lines reflect the constant grid spacing between the turbines normalized by diameter D. The wind direction flows in the positive x direction. The outlines of the overall measurement volume obtained in the inflow, between the first and second row, between the second and third row, and in the outflow (grey) are shown in dark red, blue, cyan, and grey, respectively. In the isometric view, a single measurement volume, as described in Sect. 3.3, is illustrated in the region between the second and third row. A representation of the instantaneous HFSBs is provided in this volume as well.

between the different sections of the farm (i.e. inflow, behind the first row, second row, etc.). To measure the inflow of the farm, it was assumed that the induction of the third row did not greatly impact the inflow; hence, first-row rotors were removed, and the inflow of the second row was measured and assumed to be that of the first row. As described in Sect. 2, to avoid the ground effect, the rotors are on a frame of rigid beams, resulting in a clearance between the ground and bottom blade tip of the rotor of 2.2 m ($7.3D$), as shown in Fig. 3.

3.5 Flow measurement uncertainty

Given the complexity of the measurement system, several sources of uncertainty are evident regarding the quantification of velocity in the wind farm, the most important of which are related to the overall system calibration, particle detection, and triangulation process, the signal-to-noise ratio (SNR) of the recorded images, and the quality of particle tracking and matching.

The overall system calibration and subsequent particle detection are addressed during the camera calibration phase. A geometric calibration is performed, with subsequent vol-

umetric self-calibration (Wieneke, 2008) on a reduced sample of the particle images to remove any remaining disparities between cameras, resulting in a final pixel accuracy of 0.03 px. Given the relatively low image-averaged particle seeding density of 3×10^{-2} particles per pixel (ppp), the detection and triangulation of ambiguous particles is minimized (Scarano, 2012). A threshold allowable triangulation error of 1 voxel was used to reduce ghost tracks further and improve the particle reconstruction. Pre-processed images (before background removal using the time filter described in Sect. 3.3) have an average intensity of 100 counts.

The standard deviations (σ) of the velocity components are computed over the total number of test samples of 4600. The magnitudes vary depending on the velocity component, pitch case, and wake location on the farm. Higher magnitudes in standard deviation are present in the near wake along the shear layer, as concluded in previous works of Huang et al. (2023b) and Bensason et al. (2024). These reach as high as $\sigma_x \approx 0.8\,\mathrm{m\,s^{-1}}$, $\sigma_y \approx 0.4\,\mathrm{m\,s^{-1}}$, and $\sigma_z \approx 0.3\,\mathrm{m\,s^{-1}}$ for the baseline pitch case $\beta = 0°$. Within the wake, these values drop to $\sigma_x \approx 0.17\,\mathrm{m\,s^{-1}}$, $\sigma_y \approx 0.15\,\mathrm{m\,s^{-1}}$, and $\sigma_z \approx 0.10\,\mathrm{m\,s^{-1}}$, respectively. For the pitched cases, the σ value retains a similar magnitude, with increases in the lateral and axial velocity components of up to $\sigma_y = \sigma_z \approx 0.6\,\mathrm{m\,s^{-1}}$ in the near wake within the shear layer. Within the induction region of the farm, the standard deviation of the unperturbed freestream is $\sigma_x = \sigma_y = \sigma_z = 0.05\,\mathrm{m\,s^{-1}}$ and increases in magnitude near the induction region of the first rotor row to $\sigma_x = \sigma_y = \sigma_z = 0.3\,\mathrm{m\,s^{-1}}$. The corresponding velocity uncertainty ϵ is computed using Eq. (1):

$$\epsilon = \frac{z_a \sigma_{x,y,z}}{\sqrt{N}}, \tag{1}$$

where N is the number of uncorrelated measurement samples within each bin and z_a is the coverage factor. A value of $z_a = 2$ is selected to achieve a 95 % confidence interval of the normal Gaussian distribution. Given that the 4600 recordings are considered, which are time-averaged, the number of samples per bin is on the order of 900 000. Given the selected bin size, this indicates a substantial number of samples per bin per time instance. Rather, $N = 4600$ is used as the number of uncorrelated samples per bin, which is a conservative estimate. Hence, the velocities reach a maximum of $\epsilon_x = 0.02\,\mathrm{m/s}$, which is only 0.67 % of the freestream velocity $U_\infty = 3\,\mathrm{m\,s^{-1}}$. The large number of samples per bin suggests that a higher-resolution mesh would be attainable. However, the robustness of the chosen size resolves all large-scale vortices of interest while keeping the required memory to a minimum.

Furthermore, the diffraction diameter of the particle images d_{diff} is calculated using Eq. (2) (Raffel et al., 2018):

$$d_{\mathrm{diff}} = 2.44 \times f_\# \times (M + 1) \times \lambda, \tag{2}$$

where $f_\# = 22$ is the numerical aperture and $\lambda = 500 \times 10^{-9}\,\mathrm{m}$ is the wavelength of light. The resulting diffraction diameter is $d_{\mathrm{diff}} = 27.65\,\mu\mathrm{m}$. Given the camera pixel size of 20 µm, the ratio is 1.4, which would result in minimal peak locking errors (Raffel et al., 2018).

4 Results

4.1 Rotor thrust performance

Prior to the flow-field measurements, the thrust of an isolated rotor as a function of the tip-speed ratio is measured. These results are compared to the measurements of Huang et al. (2023c), who used the same geometry with the exception of profiled struts, as described in Sect. 3.2. In this work, the tip-speed ratio is varied using rotor rotational frequency ω while keeping the inflow wind speed constant at $U_\infty = 3\,\mathrm{m\,s^{-1}}$. In the work of Huang et al. (2023c), the rotor loads were measured at an inflow speed of $U_\infty = 5\,\mathrm{m\,s^{-1}}$. The streamwise and lateral thrusts, $C_{T,x}$ and $C_{T,y}$, are defined as follows:

$$C_T = \frac{T}{0.5 \rho U_\infty^2 A}, \tag{3}$$

where T is the measured thrust component, ρ is the air density, and A is the frontal area of the rotor. The measured streamwise and lateral thrust coefficients are shown in Fig. 6 for the three pitch cases via solid lines and compared to published results (shown as dashed lines).

As with the results of Huang et al. (2023c), the streamwise thrust coefficient increases and decreases when applying a positive and negative pitch, respectively. This difference is amplified as the tip-speed ratio increases. The decrease in thrust for the negative pitch case can be attributed to the reduction in load in the intrinsically more efficient upwind passage (as described in Sect. 2). The increased load in the downwind passage does not account for that lost upwind and is further hindered by dynamic stall effects, as confirmed via blade-level measurements of LeBlanc and Ferreira (2022a) at mid-span. As reported by LeBlanc and Ferreira (2022a), the blade loads increase significantly in the UW quadrant for the positive pitch case before reducing due to stall in the UL quadrant. The streamwise thrust measurements in this campaign compare well to those published by Huang et al. (2023c) for the baseline and negative pitch cases but exhibit systematically higher values for the positive pitch case on the order of 13 % at a tip-speed ratio of 3. This discrepancy can likely be attributed to the difference in strut profile and pitch adapter design, as well as the difference in freestream wind speed and diameter based on the Reynolds number.

The lateral thrust coefficients are positive across all pitch cases, confirming the intrinsic asymmetric loading of the VAWT in favour of the windward side. For the positive pitch mode, the lateral force increases drastically compared to the baseline case by $\Delta C_{T,y} = 0.29$ (a factor of 14.3), while the negative pitch case increases by $\Delta C_{T,y} = 0.05$ (a factor of 3.8) at a tip-speed ratio of 3.5. The lateral force in the baseline case decreases as the tip-speed ratio increases, as the

Table 2. Measured thrust coefficients at tip-speed ratio $\lambda = 3.5$.

Pitch case β [°]	$C_{T,x}$	$C_{T,y}$
−10	0.72	0.386
0	0.79	0.03
10	0.92	0.10

loading between the windward and leeward halves becomes more uniform. As in the streamwise thrust case, the positive pitch shows the largest discrepancy with respect to results published by Huang et al. (2023c), which is again ascribed to the differences in the VAWT models and the Reynolds numbers. For the results presented, a constant tip-speed ratio of $\lambda = 3.5$ was maintained, with the thrust coefficients tabulated in Table 2.

4.2 Streamwise vorticity system

As discussed in Sect. 2, the wake topology is governed by the modified trailing vorticity system of the rotor when in vortex generator mode. The iso-surfaces of the normalized streamwise vorticity $\omega_x D/U_\infty$ are shown for the three modes of operation in Fig. 7, calculated using a three-point central finite difference scheme. The values are flooded by $\omega_x D/U_\infty = \pm 1$ for the vortex generator modes and $\omega_x D/U_\infty = \pm 0.4$ for the baseline case. The lateral and axial vorticity contours are presented in Appendix B for completeness. Furthermore, the normalized vorticity at discrete cross-stream locations $x/D = 2.5$, 7.5, and 12.5 is presented in Fig. 8. The vectors show the in-plane velocities, and the solid black line indicates the projected frontal area of the central rotor column. The dominant vortical structures stemming from the respective AC quadrants are labelled, following the same naming convention described in Sect. 2. The label "S" corresponds to structures stemming from the interfaces between the struts and blade. Given the symmetry about the $z/D = 0$ plane, only the structures on the upper half of the wake are labelled.

For the baseline case, there are no dominant vortical structures stemming from the AC quadrants behind the first rotor $x/D = 2.5$, with the presence of both upwind- and downwind-generated vortices on the windward and leeward sides. The UW vortex persists longer in the wake, reaching the second rotor, whereas the DW extends up to approximately $x/D = 3$, confirming the intrinsically higher load of the upwind half. Similarly, on the leeward half of the rotor, the UL vortex persists until the second rotor in the column. The intrinsically higher load and the windward half of the cycle are further highlighted by the difference in sizes of these vortical structures as they convect through the wake. In addition to the quadrant-based vortical structures, streamwise vorticity due to the struts is present. The same structures were observed by Huang et al. (2023b) and persist both on the windward and leeward sides. The streamwise vorticity structure behind the second rotor is analogous to that of a bluff body cylinder (Schneiders et al., 2016), with dominant anti-clockwise and clockwise rotating structures on the windward and leeward sides, respectively. These structures induce a significant axial contraction of the wake, evidenced by the induced downwash and upwash on the upper and lower halves, respectively. As the inflow velocity of the second rotor has been reduced significantly (as evidenced in Sect. 4.3), the effective tip-speed ratio of the rotor will increase significantly (as the rotational frequency is kept constant), as well as the thrust coefficient. The structures persist in the wake until reaching the third rotor in the column. Behind the third rotor at $x/D = 12.5$, the same structures persist but at much lower strengths, as evidenced in the iso-surfaces.

For the positive pitch case $\beta = 10°$, the dominant vortical structures are those generated on the upwind half of the cycle, namely, the UW and UL as seen at $x/D = 2.5$, as discussed in Sect. 2. The UW structure is larger than the UL structure due to the higher load on the windward side. Due to the significant lateral force induced on the wake when pitching the blades, the structures convect towards the windward side. Those generated on the UW quadrant convect more due to their higher strength. Unlike the baseline case, the inflow for the second rotor recovers to a much higher degree due to the injection of high-momentum flow from above the rotor, and hence it exhibits a similar vortical structure to that of the first rotor. The UW-generated vortex for the rotor on the neighbouring column has convected within the measurement volume, at around $y/D = -2.0$ at $x/D = 7.5$. Compared to the structures of the first rotor, the UL vortices have convected further inside the projected frontal area. Finally, behind the third rotor at $x/D = 12.5$, three UW-generated vortices are present in the measurement volume, namely, those generated by the second and third rotors in the column, as well as the second rotor in the neighbouring column on the leeward side. As seen in the iso-surfaces, the flooded structures generated by the third rotor do not extend as far as those generated by the second, suggesting a weaker structure and an accelerated diffusion. This is likely a result of the decrease in rotor load, linked to the inflow of the ejected wake from the leeward side columns, as discussed in Sect. 4.3.

Finally, for the negative pitch case, the dominant vortical structures in the wake are generated in the DW and DL quadrants. Behind the first rotor at $x/D = 2.5$, the DW structure remains concentrated around the upper blade tip, while that on the DL convects within the projected area of the rotor. The CVP on the leeward side induces a lateral injection of high-momentum flow into the wake. As in the baseline pitch case, vortices generated by the struts are apparent, albeit only on the leeward side. Behind the second rotor at $x/D = 7.5$, the same dominant structures persist, with seemingly higher strengths. The DW-generated vortex has convected above and towards the centre axis of the rotor, while the DL has spread across the entire diameter of the rotor. The CVP between the upper and lower blades on the leeward side

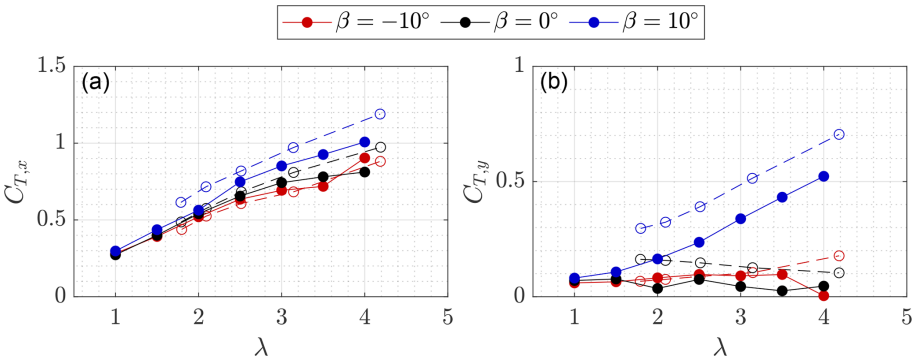

Figure 6. Streamwise **(a)** and lateral **(b)** thrust coefficients as a function of tip-speed ratio for the three thrust coefficients. The solid and dashed lines correspond to recorded results from this experiment and those reported by Huang et al. (2023b), respectively. All measurements of this experiment are recorded at a constant wind speed of 3 m s^{-1}.

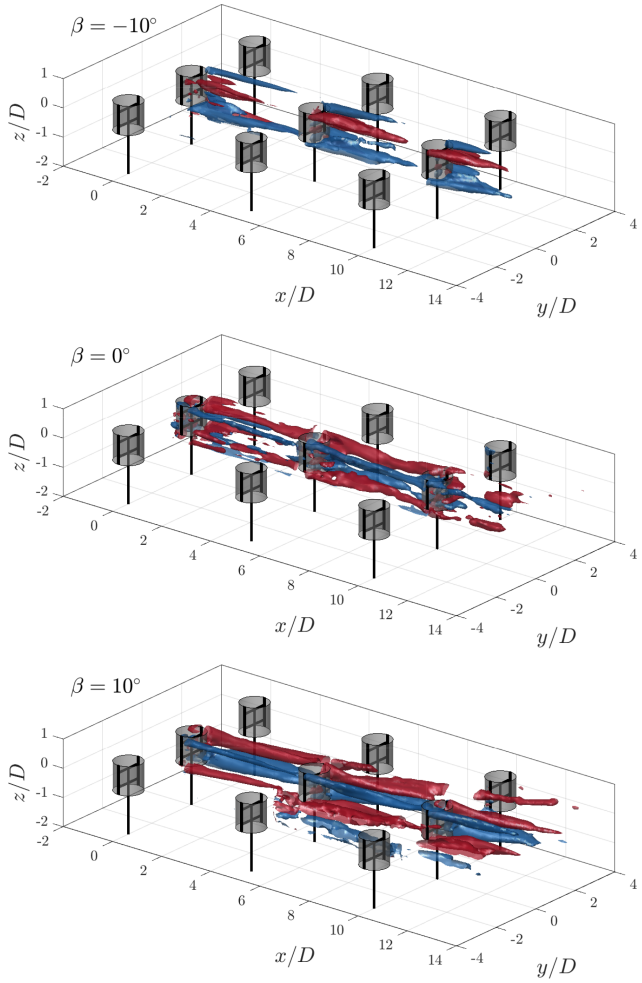

Figure 7. Iso-surfaces of the streamwise vorticity contours at $\omega_x D/U_\infty = \pm 1$ for pitch cases $\beta = \pm 10°$ and at $\omega_x D/U_\infty = \pm 0.4$ for $\beta = 0°$. The rotors are shown at a $\theta = 0°$ phase, with the grey-shaded cylinders representing the idealized actuator cylinder load.

induces a significant injection of momentum into the wake while ejecting the wake out from the windward side. Behind their rotor at $x/D = 12.5$, the same behaviour persists. As in the case of the positive pitch blades, the vortical structures do not extend as far in the wake as in the aforementioned volumes, presumably due to the lower thrust of the third rotor and increased turbulence further in the wind farm wake.

4.3 Wake topology

As discussed in Sect. 2, the streamwise vorticity system is an important driver of the wake topology. The normalized streamwise flow component U_x/U_∞ is shown as iso-surfaces in Fig. 9 for the baseline and vortex generator mode cases. The normalized streamwise flow is flooded at values $U_x/U_\infty = 0.9$ and 0.5, shown in orange and blue, respectively. The swept volumes of the rotors are shaded grey to represent the idealized actuator cylinder surface. Furthermore, the wake at discrete cross-stream distances $x/D = 2.5$, 7.5, and 12.5 is shown in Fig. 10 for the same cases. Finally, the normalized streamwise velocity component at the symmetry planes $y/D = 0$ and $z/D = 0$ are shown in Figs. 11 and 12, respectively. In-plane velocity vectors are shown for all cases. The contours at the symmetry plane $y/D = 0$ include the wake boundary at $U_x/U_\infty = 0.6$. The contours at the symmetry plane $z/D = 0$ show the wake centre via a white line, calculated using the centre of mass approach (Howland et al., 2016), as shown in Eq. (4):

$$y_c(x) = \frac{\iint y \Delta U(x,y,z)\mathrm{d}y\mathrm{d}z}{\iint \Delta U(x,y,z)\mathrm{d}y\mathrm{d}z}, \tag{4}$$

where $\Delta U(x,y,z) = U_\infty - U_x(x,y,z)$. The integration is performed at discrete cross-stream planes x/D. As the wake is symmetric about $z/D = 0$, the integration domain is constrained to $z/D \geq 0$ such that the available data are consistent across all pitch cases. For the baseline and negative pitch cases, the lateral domain is constrained to $-1.6 \leq y/D \leq 1.6$. In contrast, the positive pitch case is constrained to

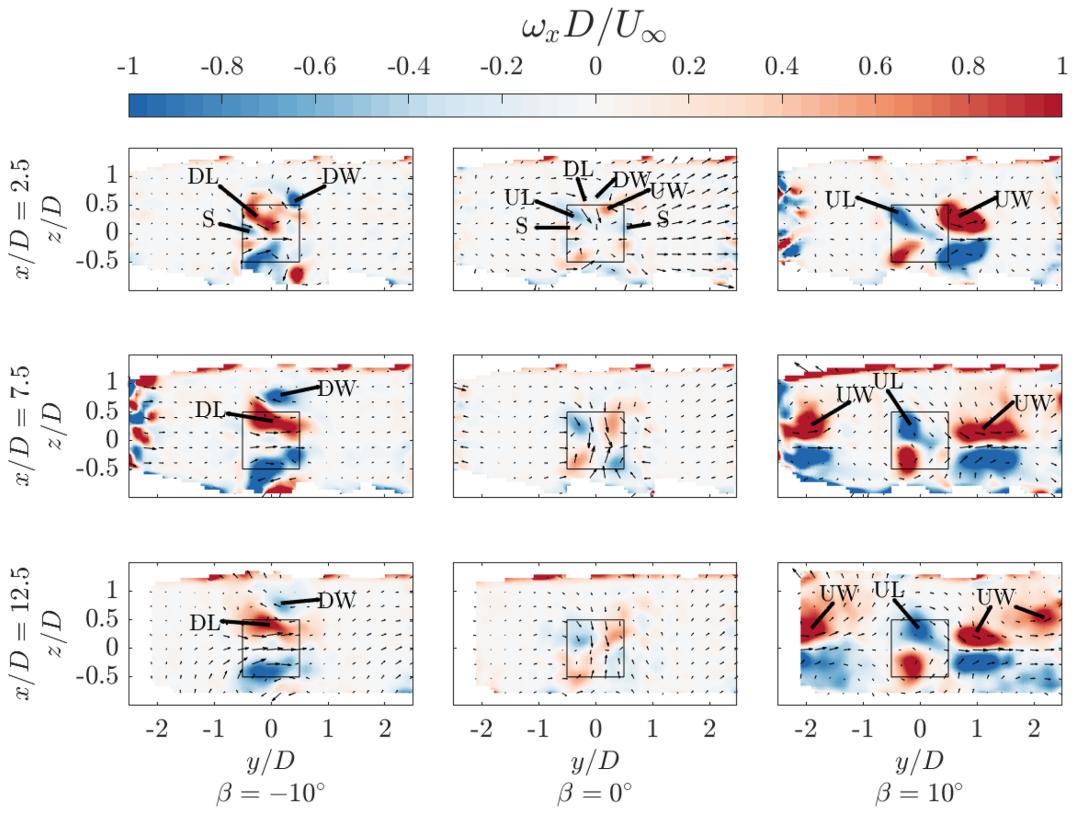

Figure 8. Normalized streamwise vorticity at $\omega_x D/U_\infty$ for the three pitch cases at streamwise locations $x/D = 2.5$, 7.5, and 12.5. The black-outlined square indicates the projected frontal area of the rotors, and the vectors show the in-plane velocity components. The streamwise vortical structures generated by each AC load quadrant are labelled, as described in Sect. 2. The label "S" corresponds to structures generated at the interface between the struts and blade.

$-0.75 \leq y/D \leq 2.3$ to limit the impact of the wakes of the neighbouring column on the computation. Beyond the third rotor's wake $x/D > 10$, the wakes between the central column and neighbouring column rotors combine and become difficult to separate.

The baseline case $\beta = 0°$ exhibits the most significant flow deficit, evident by the largest blue-flooded region in the iso-surfaces and blue area in the cross-stream plane $x/D = 2.5$. The cross-stream plane confirms the asymmetric load profile of the rotor, with an asymmetric wake directed towards the windward side. Similar topologies have been experimentally measured by Huang et al. (2023b) and Rolin and Porté-Agel (2018). This asymmetry grows as the wake progresses downstream, as seen by the deformation of the blue-shaded wake core at $U_x = 0.5$, as well as the wake centre line in Fig. 12. The wake at the symmetry plane $y/D = 0$ exhibits a maximum flow deficit at approximately $x/D = 2.5$, at which point a gradual wake contraction occurs in the axial direction, evidenced by the in-plane vectors. The second and third rotors in the column are immersed in the wakes of the upstream rotors, evidenced by the extension of the orange-flooded regions within the measurement volumes. The flow at the symmetry planes has a gradually shorter wake length for the second and third rotors in the column, presumably due to decreased rotor thrust with a lower inflow velocity, as seen in Fig. 12. The asymmetry in the wake grows throughout the farm, as seen at $x/D = 7.5$ and 12.5, with larger regions of flow deficit concentrated on the windward sides of the rotor. As there is no major lateral force component, as shown in Sect. 4.1, the wakes of the surrounding columns do not become visible in the measurement domain until towards the end of the farm volume. As discussed in reference to the streamwise vorticity, the axial contraction of the wake at the symmetry plane $y/D = 0$ increases significantly behind the second and third rotors in the column. In contrast, the width of the wake in the lateral direction grows as the wakes superimpose.

For the positive pitch case $\beta = 10°$, a significant lateral deflection of the wake towards the windward side is evident from the iso-surfaces and cross-stream plane $x/D = 2.5$. This is consistent with the significant increase in the measured lateral force of an isolated rotor, as discussed in Sect. 4.1. In addition to the lateral wake deflection, there is a significant axial contraction of the wake due to the influx of high-momentum flow from above and below the rotor. The work of Huang et al. (2023b) demonstrates a similar wake topology. The wake contraction is evident by the cross-

stream planes, and a significant decrease in wake length is seen at the symmetry plane $y/D = 0$. This significant wake re-energization is also evident in the reduction in blue-shaded regions of the iso-surfaces compared to the baseline operating case. Given the recovered incoming flow for the second rotor, the wake deflection process is still effective, as seen from the symmetry plane $z/D = 0$. Also evident is the appearance of the deflected wake in the measurement domain from the neighbouring column on the leeward side, starting at approximately $x/D = 2$. These wakes continue to travel laterally within the measurement volume and impinge on the third rotor in the column, as seen by the iso-surfaces and the cross-stream plane at $x/D = 12.5$. The wake centre line gradually approaches $y_c/D = 0$ behind the third rotor as the wake from the neighbouring column on the windward side enters the projected frontal area of the central rotors.

Finally, for the negative pitch case $\beta = -10°$, the wake is re-energized from the sides while ejecting low-momentum flow out from above and below the rotor, evident by the elongated wake shape in the axial direction in Fig. 9 and cross-stream plane $x/D = 2.5$. The injection of momentum laterally is asymmetric in favour of the leeward side and grows as the wake progresses in the farm, as seen at cross-stream planes $x/D = 7.5$ and $x/D = 12.5$. This follows the discussion of the modification and convection of the dominant downwind vortices in Sect. 4.2. This mode of operation is clear when observing the flow at the symmetry plane $y/D = 0$, with gradual growth in flow deficit above and below the rotor plane, while flow is re-energized at the wake rotor centre plane. The wake at the symmetry plane $z/D = 0$ confirms the measured increase in the lateral load of the rotor, as seen by the deflection of the wake towards the windward side. However, when considering the entire cross-section of the wake, the wake centre line is concentrated around $y_c/D = 0$. This is due to the portion of the wake that has been ejected out axially above the rotor, which connects gradually towards the leeward side, as seen in the cross-stream planes.

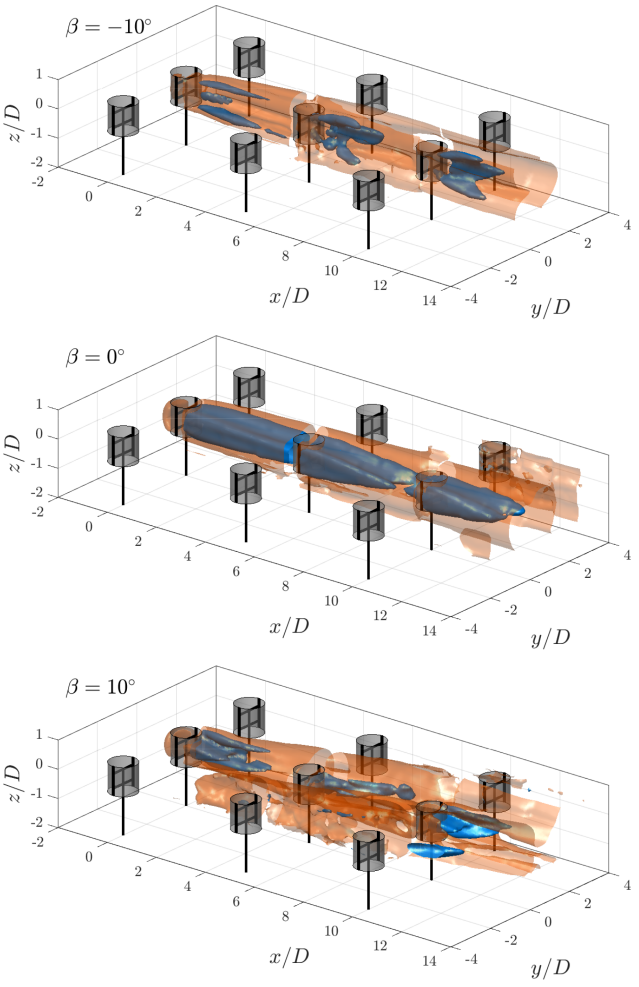

Figure 9. Iso-surfaces of the normalized streamwise velocity $U_x/U_\infty = 0.5$ and 0.9 in blue and orange, respectively, for the three pitch cases. The rotors are shown at a phase-locked position $\theta = 0°$, with the grey-shaded cylinders representing the idealized actuator cylinder load.

4.4 Wake recovery

The contours shown in Sect. 4.3 give a qualitative indication of the wake recovery mechanism of the vortex generator modes. To indicate the quantitative recovery of streamwise velocity in the wake, the normalized streamwise velocity deficits $1-(U_x/U_\infty)$ at symmetry plane $y/D = 0$ and cross-stream planes $x/D = 2.5$, 7.5, and 12.5, each $2.5D$ from the central column rotors, are shown in Fig. 13. In addition, the lateral average of the velocity within the projected regions of $-0.5 \le y/D \le 0.5$ (projected frontal area) and $-1.6 \le y/D \le 1.6$ (central column grid size) are presented, denoted as $y/D \pm 0.5$ and $y/D \pm 1.6$, respectively. Additionally, the normalized axial velocity component U_z/U_∞ for each case is presented.

The streamwise velocity distributions about the symmetry plane $y/D = 0$ confirm the vortex generator mode of operations discussed in Sect. 2. For the baseline case, there is a large deficit behind the first rotor in the column, reaching $1-(U_x/U_\infty) = 1.1$, suggesting a small region of backflow in the wake, visible in Fig. 11. The deficits are lower behind the second and third rotors because the rotors produce less thrust, yielding shorter wake lengths, as discussed in Sect. 4.3. The maximum deficits behind the second and third rotor are $1-(U_x/U_\infty) = 0.63$ and $1-(U_x/U_\infty) = 0.6$, respectively. The profiles for all three cross-stream locations are relatively symmetric about the $z/D = 0$ plane with minor differences due to the rotor tower, consistent with the discussion in Sect. 2. The axial velocity behind the first rotor at $x/D = 2.5$ is low in magnitude and reaches a local minimum of $U_z/U_\infty = -0.04$ near the rotor tips, suggesting a wake expansion. Behind the second and third rotors, the profile approaches that of the positive pitch case, suggesting a

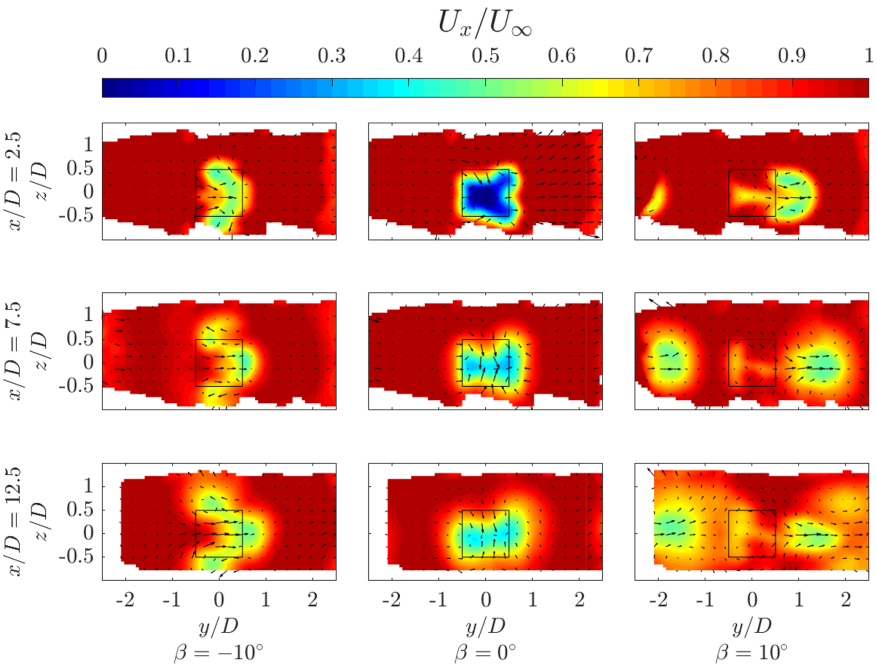

Figure 10. Normalized streamwise velocity U_x/U_∞ for the three pitch cases at streamwise locations $x/D = 2.5$, 7.5, and 12.5. The black-outlined square denotes the projected frontal area of the rotor, and the vectors show the in-plane velocity components.

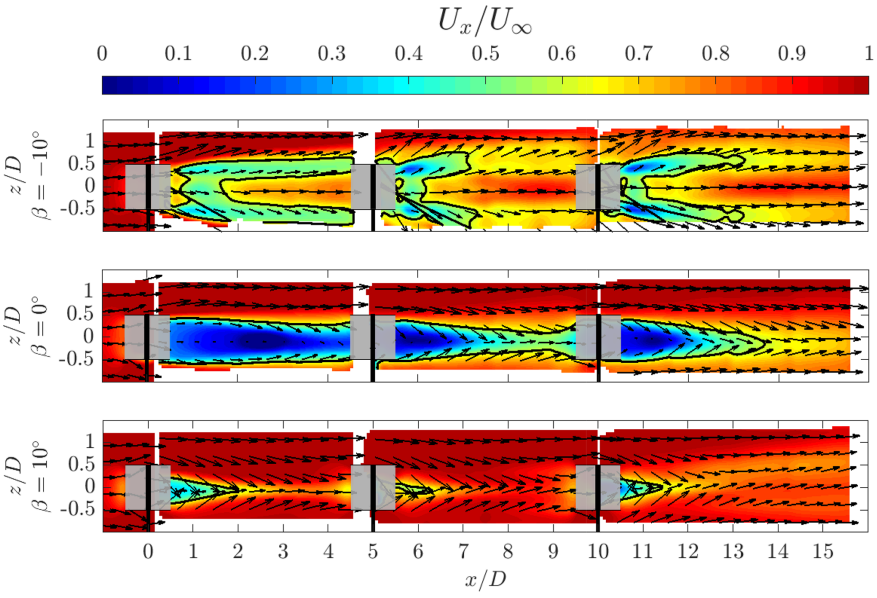

Figure 11. Normalized streamwise velocity U_x/U_∞ for the three pitch cases at the constant lateral plane $y/D = 0$. The vectors show the in-plane velocity components. The thick black line denotes the wake boundary at $U_x/U_\infty = 0.6$. The grey-shaded squares represent the idealized actuator load surface, and the black volumes show the rotor at a phase of $\theta = 0°$.

significant wake contraction, as discussed in Sect. 4.3, with minima of $U_z/U_\infty = -0.16$ in the upper half.

For the vortex generator mode with negative pitch $\beta = -10°$, the flow behind the first rotor is substantially recovered compared to the baseline case within the range $-0.5 \leq z/D \leq 0.3$, reaching a maximum deficit of $1 - (U_x/U_\infty) = 0.26$. As the wake is ejected out axially above and below the rotor, as suggested by the U_z/U_∞ profile, the flow deficits above and below the projected frontal area of the rotor are greater than the baseline case, reaching $1 - (U_x/U_\infty) = 0.5$. The wake region extends up to a height of $z/D = 0.9$ compared to the baseline case of $z/D = 0.6$, with a maximum up-

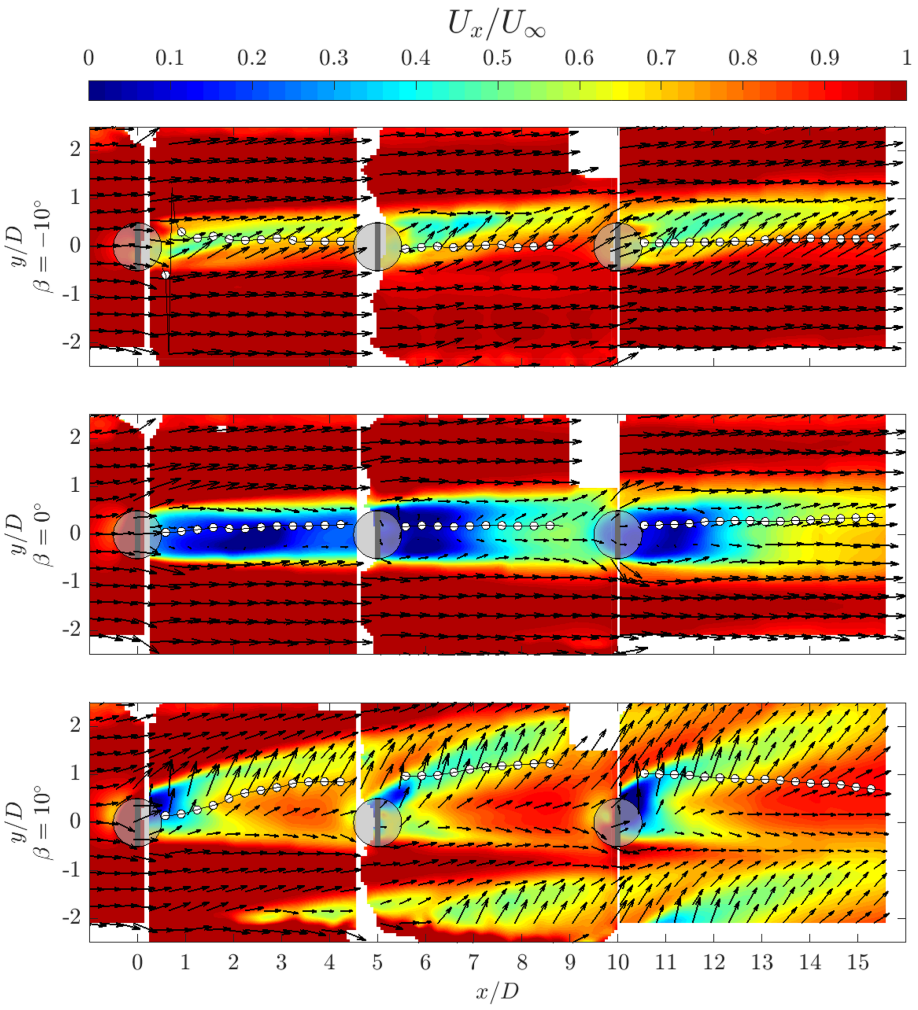

Figure 12. Normalized streamwise velocity U_x/U_∞ for the three pitch cases at the constant axial plane $z/D = 0$. The vectors show the in-plane velocity components. The white markers show the wake centre as computed using Eq. (4). The grey-shaded squares represent the idealized actuator load surface, and the black volumes show the rotor at a phase of $\theta = 0°$.

wash of $U_z/U_\infty = 0.1$ above the rotor plane. Behind the second rotor, the maximum deficit decreases to $1-(U_x/U_\infty) = 0.12$. The wake region continues to expand above and below the rotor, encompassing a larger range above $z/D = 1.3$, while reaching a lower maximum deficit of $1-(U_x/U_\infty) = 0.34$. Behind the third rotor, the wake region expands even further above the area of the rotor and reaches a maximum deficit within the bounds of the rotor of $1-(U_x/U_\infty) = 0.23$. The maximum upwash decreases between the cross-stream planes $x/D = 7.5$ and 12.5 from $U_z/U_\infty = 0.16$ to 0.1, respectively. This is due to the decrease in vortex strength, as seen in Fig. 8.

Finally, for the vortex generator mode with positive pitch $\beta = 10°$, the wake is axially contracted while ejected out laterally. Hence, a significant reduction in the streamwise flow deficit behind the first rotor is evident, with a maximum deficit of $1-(U_x/U_\infty) = 0.32$. The wake region has also contracted, reaching a height of $z/D = 0.3$, suggesting freestream flow within the projected frontal of the rotor, highlighted in Fig. 11. The downwash on the upper half of the rotor reaches a local minimum of $U_z/U_\infty = -0.2$. Behind the second rotor, the maximum wake deficit decreases to $1-(U_x/U_\infty) = 0.17$ while maintaining a similar wake width. The local minima of the downwash remain similar, with $U_z/U_\infty = -0.18$. The location of this minima shifts due to the larger deflection of the wake behind the second rotor, as seen in Fig. 12. The symmetry above and below the rotor begins to deviate behind the third rotor as the wakes of the rotors on the neighbouring column enter the measurement volume, as shown in Fig. 10. Similarly, the maximum magnitudes of the downwash and upwash on the upper and lower halves of the wake deviate, presumably due to the different lateral locations of the UL vortices, as shown in Fig. 8.

When taking the lateral average within the projected frontal area of the rotor $-0.5 \leq y/D \leq 0.5$, the trend is similar to the non-averaged profile. The baseline case exhibits the

highest flow deficit across all three measurement planes, with similar maximum deficits behind the second and third rotors. For the negative pitching case $\beta = -10°$, the mean streamwise velocity recovery within the projected frontal area of the rotor is higher than the baseline case across the three measurement planes. As described in the aforementioned case, the wake is ejected out axially above and below the rotor, leading to higher average deficits within the extended lateral domain beyond $z/D \geq 0.5$ compared with the baseline case. The profile does not exhibit as notable peaks in the streamwise flow deficit above and below the rotor as with the profile from the symmetry plane $y/D = 0$. Finally, for the positive pitch case $\beta = 10°$, the trend is similar to that on the symmetry plane. The axial flow profiles also maintain a similar trend to the non-averaged case. However, a clear difference appears for the positive pitch case, where the maximum magnitude decreases more rapidly between the cross-stream planes, from $U_z/U_\infty = 0.13$ to 0.02 at $x/D = 2.5$ and 12.5, respectively. This can be attributed to the gradual convection of the UL vortices within the projected volume of the rotors.

When extending the domain for the lateral average to $-1.6 \leq y/D \leq 1.6$, the relationships between the three modes of operation begin to deviate from the aforementioned cases. In general, the deficits increase downstream as the wakes superimpose and the deflected wakes from the neighbouring columns enter the extended domain. Behind the first rotor, the baseline case $\beta = 0°$ exhibits the highest deficit, with $< 1 - (U_x/U_\infty) >= 0.3$. However, due to the extended domain in the lateral direction, the negative pitch case $\beta = -10°$ exhibits the highest wake recovery, with $< 1 - (U_x/U_\infty) >= 0.1$, compared to the positive pitch case $\beta = 10°$, with $< 1 - (U_x/U_\infty) >= 0.19$. This is because the ejected wake of the positive pitch mode of operation falls within the extended lateral range, whereas the axially ejected wake of the negative pitch mode falls outside the integration window. Behind the second rotor, the relationship between the three modes of operation remains the same, with higher maximum streamwise deficits. The maximum deficits between the positive pitch case and baseline become more similar as the wakes from the surrounding columns deflect within the interrogation volume. Finally, behind the third rotor, the maximum flow deficits for the baseline and positive pitch case are very close in magnitude, with $< 1 - (U_x/U_\infty) >= 0.33$ and $< 1 - (U_x/U_\infty) >= 0.31$, respectively. This is attributed to the deflected wakes from the neighbouring column for the positive pitch case, as seen in Fig. 12.

4.5 Available power

The flow-field contours shown in Sect. 4.3 visually confirm the injection of high-momentum flow into the wake for both vortex generator modes, given the availability of freestream inflow for the second and third rotors in the central column. To further highlight the efficacy of these modes of operation on the replenishment of kinetic energy in the wake, the potentially available power (AP) in the wake is quantified at a selected cross-stream location using the coefficient of available power f_{AP}. A similar analysis was performed by Huang et al. (2023b), Bossuyt et al. (2021), and Hezaveh and Bou-Zeid (2018a) to highlight the replenishment of high-momentum flow inside a selected domain and is computed as:

$$f_{AP}(x, y_0, z_0) = \iint_S U_x^3(x, y, z)/U_\infty^3 \mathrm{d}z\mathrm{d}y, \tag{5}$$

where U_x^3/U_∞^3 is the coefficient of available power at a select cross-stream plane x. The surface integral is computed within a defined domain (S), which is centred at y_0, z_0 in the lateral and axial directions, respectively. The available power coefficients throughout the central column of the wind farm are shown in Fig. 14 for the three modes of operation. The average available power is computed within the projected frontal area of the central column rotors $y_0/D = z_0/D = 0$. The vertical dashed lines indicate the boundaries of the rotor-swept areas for the central column. Note that, as the powers of the rotors in the farm were not measured, the presented curves are not scaled to account for the extracted power from the flow of the rotors within the central column.

For the baseline case within the projected frontal area of the rotor, the available power does not surpass 20 % between the first and second rows. The AP reaches a minimum of $< U_x^3/U_\infty^3 >= 0.06$ at $x/D = 1.4$ before steadily recovering due to the inherent diffusion of the wake. Between the second and third row, the AP recovers much faster, consistent with the shorter wake length observed in Figs. 11 and 12, as well as the lower recorded thrust coefficient of the second rotor. The AP reaches a maximum of 0.25 at $x/D = 9$ before decreasing upstream of the third rotor in the column due to its induction. Finally, downstream of the third rotor, the AP increases at a rate similar to that of the previous case, reaching a recorded maximum of 0.42 at $x/D = 15.5$.

For both vortex generator control strategies, the available power in the wake is higher than in the baseline case within the projected frontal area of the rotor. The case where momentum is injected from above the rotor $\beta = 10°$ exhibits higher AP across all measurement domains compared to the alternative case of $\beta = -10°$. Directly behind the first rotor, the negative pitch case reaches a minimum AP of 0.32 at $x/D = 1.3$ before gradually increasing. The positive pitch case reaches a maximum AP of 0.72 at $x/D = 3.2$ before a steep drop due to the amplified induction of the second rotor. This drop due to induction is not as visible in the negative pitch case, as the load shifted from the upwind quadrant. Between the second and third rotors, the AP is higher directly downstream of the rotor for the positive pitch case compared to the aforementioned volume. However, a comparable maximum AP of 0.7 is reached at a similar distance from the rotor of $x/D = 8.4$ before dropping due to the induction of the third rotor. Contrarily, the negative pitch case

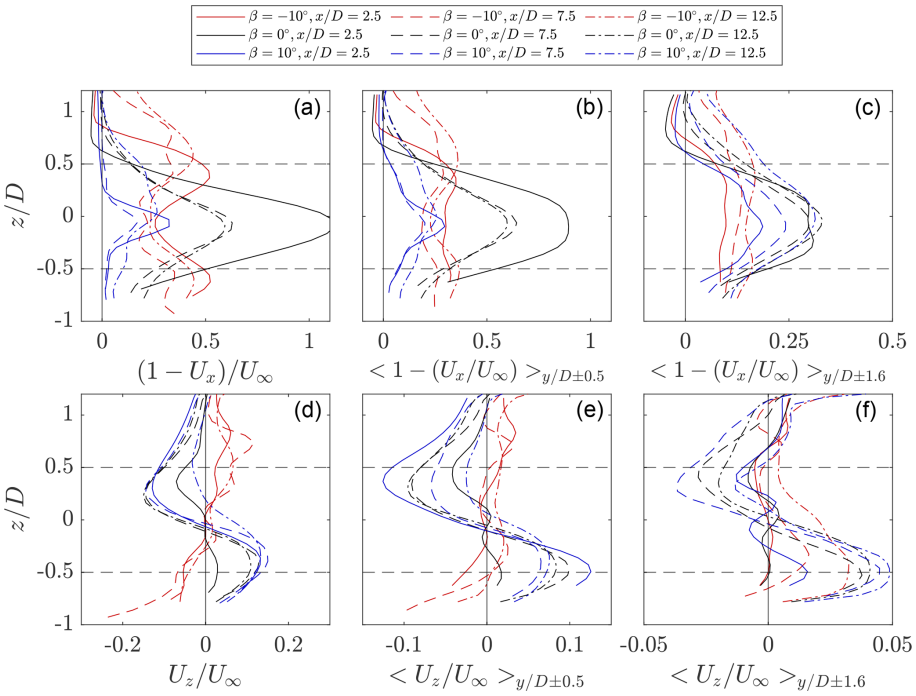

Figure 13. Normalized streamwise deficit $1-(U_x/U_\infty)$ and axial U_z/U_∞ velocity profiles at discrete cross-stream measurement planes $x/D = 2.5$, 7.5, and 12.5 for the vortex generator and baseline modes of operations. **(a, d)** The normalized velocity profiles about the $y/D = 0$ symmetry plane. **(b, e)** Lateral-averaged streamwise velocity profiles within the projected frontal area of the rotor $-0.5 \leq y/D \leq 0.5$. **(c, f)** Lateral-averaged velocity profiles within the lateral domain $-1.6 \leq y/D \leq 1.6$. The horizontal dashed lines indicate the upper and lower bounds of the rotor's projected frontal area.

reaches a higher maximum compared to the previous volume of AP = 0.53 at $x/D = 8.7$. Finally, behind the third rotor, the positive pitch case shows overall lower AP compared to the previous volumes. Inspection of the flow fields in Sect. 4.3 sheds light on the reason why the deflected wakes from the side columns have entered the domain directly downstream of the third rotor of the central column. Conversely, the negative pitch case shows a similar rate of increase in AP compared to the aforementioned volume, as the wakes from the side columns deflect far less compared to the positive pitch case, reaching a comparable AP of 0.54 at the final measurement location of $x/D = 15.5$.

To shed light on the potential optimal placement of further downstream turbines with the freedom to have lateral offsets, the AP coefficient is computed within the projected frontal area of the rotor centred at different lateral offsets to $-1.5 \leq y_0 \leq 1.5$ over all streamwise measurement planes. These are presented as a contour plot in Fig. 15 for the three modes of operation, where the solid black line indicates where $f_{AP} = 0.7$, i.e. a 70 % recovery of the maximum AP from the streamwise flow. Furthermore, the sliding window AP is extracted at three discrete streamwise locations $x/D = 2.5$, 7.5, and 12.5 for the three modes of operation, as shown in Fig. 16.

For the baseline case, the wake is concentrated within the projected frontal area of the rotor, with beyond 70 % AP on the windward and leeward sides of the rotor. The AP distribution is slightly asymmetric, with more of a deficit on the windward side of the rotor. This is consistent with the asymmetric loading of the rotor described in Sect. 2. Behind the second and third rows, the depleted energy regions grow on either side of the rotor as the wakes superimpose on each other, as seen in Fig. 16 by the gradually flattening curves and diminishing maximum AP deficits, increasing from 0.08 at $x/D = 2.5$ to 0.2 at $x/D = 12.5$. For the negative pitch case, where momentum is entrained through the sides of the rotor, the region where AP falls below 70 % is narrower, as the wake is ejected out of the volume axially. Consistent with the increase in the lateral load shown in Sect. 4.1, the wake deflects towards the windward side, yielding lower AP potential for rotor positions in that direction. The AP is higher than that of the baseline case across all lateral positions, as shown in Fig. 16. Finally, for the positive pitch case, the regions of AP below 70 % are deflected towards the windward side of the rotor, yielding a large region in the leeward side where a potential rotor can experience close to 100 % of the AP. Within the range of $-0.6 \leq y_0/D \leq 0.4$, the AP of the positive pitch case is higher than the other two modes of operation, beyond which lower AP occurs on the windward side. Behind the second rotor, the wake of the rotor in the first row persists on the windward side. On the leeward side, the region of high potential AP is smaller due to the wake of the rotors

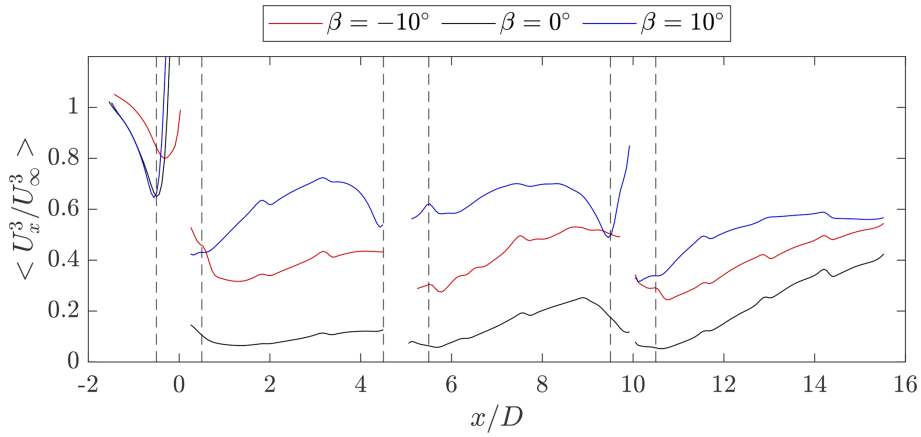

Figure 14. Mean available power $< U_x^3/U_\infty^3 >$ as calculated using Eq. (5) for the three pitch cases over the streamwise distance x/D within the projected frontal area of the central rotor column $-0.5 < z/D, y/D < 0.5$. The vertical black dashed lines correspond to the boundaries of the swept volumes of the central column rotors.

in the neighbouring column. Finally, behind the third rotor, the region where the AP surpasses 70 % is again reduced between the wakes of the third rotor and neighbouring columns. This mode of wake recovery yields higher AP at $x/D = 12.5$ in a narrow lateral spacing window of $-0.1 \leq y_0/D \leq 0.9$.

4.6 Surface momentum flux

The discussion in Sect. 4.5 highlighted the potential for increased energy density of a VAWT farm using a wake recovery strategy. To help quantify the process of wake recovery, a volume analysis of the energy equation is adopted. Similar techniques have been used by Hezaveh and Bou-Zeid (2018a) and Cortina et al. (2016), while Huang et al. (2023b) and Bossuyt et al. (2021) used the momentum equation terms to highlight the recovery processes of individual VAWTs and HAWTs. The mean kinetic energy (MKE) equation can be derived from the momentum equation and is formulated as (Hezaveh and Bou-Zeid, 2018a):

$$\frac{\partial\left(\frac{1}{2}U_x^3\right)}{\partial x} = -\frac{\partial\left(\frac{1}{2}U_y U_x^2\right)}{\partial y} - \frac{\partial\left(\frac{1}{2}U_z U_x^2\right)}{\partial z} - U_x\frac{\partial\left(\overline{U_x'U_x'}\right)}{\partial x} - U_x\frac{\partial\left(\overline{U_x'U_y'}\right)}{\partial y} - U_x\frac{\partial\left(\overline{U_x'U_z'}\right)}{\partial z}. \quad (6)$$

The expressions denoted with primes are the fluctuations of the temporally averaged velocity components in each direction with subscripts x, y, z. As in the work of Huang et al. (2023b) and Bossuyt et al. (2021), the equation is rearranged to equate the advective and Reynolds stress contributions towards the streamwise energy recovery term. The viscous forces are neglected due to the sufficiently high diameter-based Reynolds number. The pressure term is omitted, as it

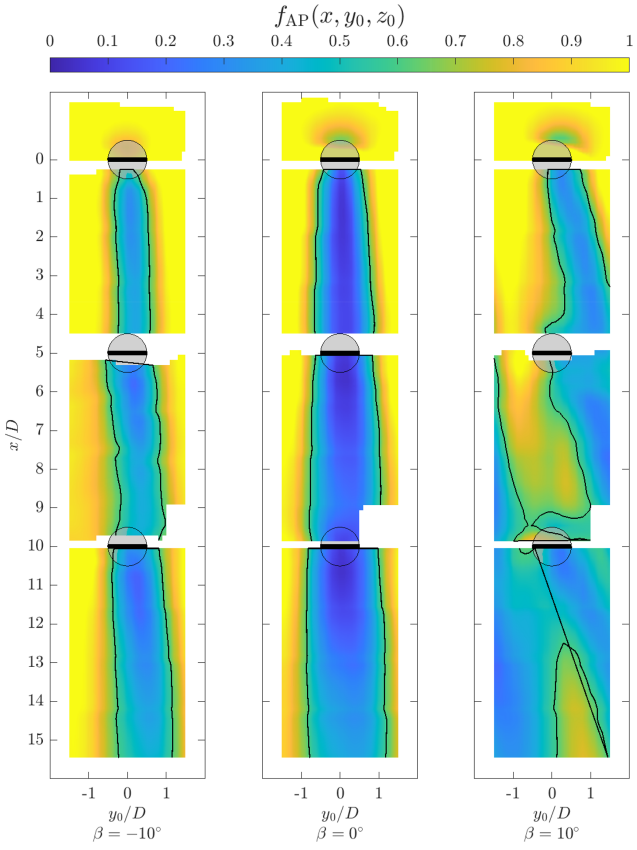

Figure 15. Available power as calculated using Eq. (5) for the three pitch cases over all streamwise distances x/D and lateral offsets y_0/D ranging from -1.5 to 1.5. The grey areas indicate the top-view areas of the rotor and the idealized actuator surface. The black contour lines show where $f_{AP} = 0.7$, i.e. 70 % of the maximum available power is provided by the streamwise flow.

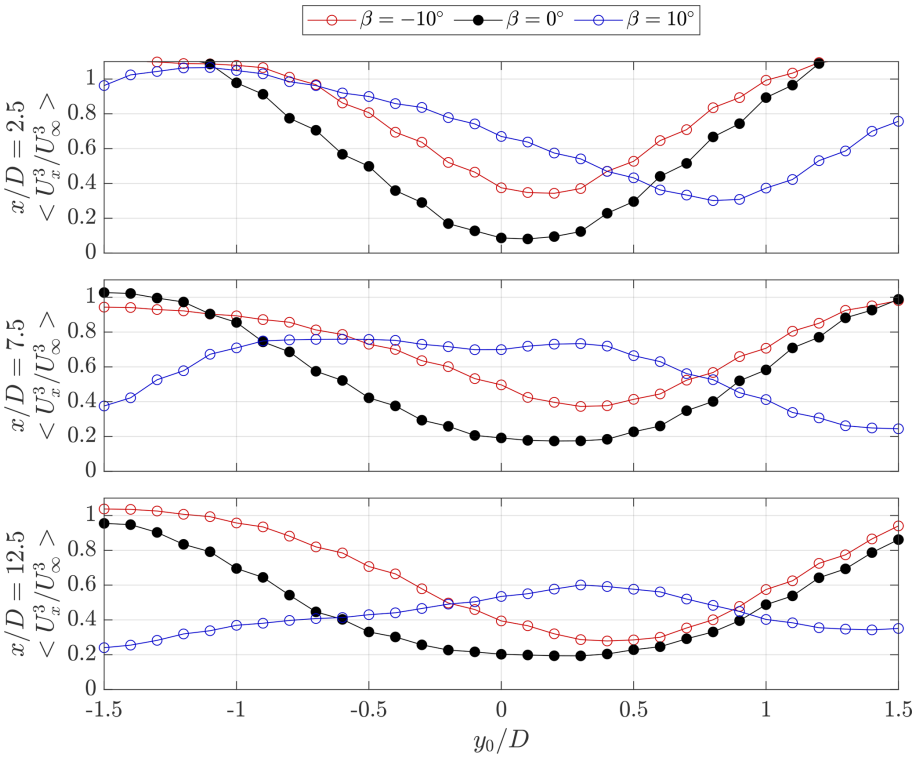

Figure 16. Available power as calculated using Eq. (5) for the three pitch cases at discrete streamwise distances x/D of 2.5, 7.5, and 12. The AP is computed within the projected frontal area of the rotor $-0.5 < z/D, y/D < 0.5$ with a lateral centre y_0 and with the discrete measurement plane.

was not measured. Furthermore, terms regarding the Coriolis, thermal buoyancy, and turbine forcing as considered in the work of Cortina et al. (2016) are exempted from this examination of the driving advective process of the streamwise vorticity system.

To investigate the relative contributions of the aforementioned terms towards wake re-energizing within the wind farm, a control volume analysis is adopted, as in the works of Cortina et al. (2016) and Hezaveh and Bou-Zeid (2018a). The proposed control volume is illustrated in Fig. 17. The volume encompasses the entire measurement domain in the streamwise direction, ranging between $-2 \leq x/D \leq 16$. The upper and lower surfaces of the control volume are taken as the heights of the upper and lower blade tips $-0.5 \leq z/D \leq 0.5$. Finally, the lateral size is taken as the diameter of the wind turbines, with $-0.5 \leq y/D \leq 0.5$. Given the limited measurement domain in the axial direction, this ensures that an equal surface area is considered for the flux on the axial and lateral surfaces. As the mean kinetic energy along the streamwise direction is the most critical towards turbine performance, the focus is placed on the flux of energy lateral and axial surfaces, while the inflow and outflow surfaces (S_1 and S_2, respectively) are omitted from the subsequent analysis.

Following the procedure outlined by Cortina et al. (2016), the volume integral of the terms in Eq. (6) can be simplified by applying the divergence theorem to rewrite the terms to a surface integral form. This is simplified further by considering that velocities normal to the surfaces do not contribute to the flux. Hence, the fluxes through the normals of the control surfaces $S_{3,4,5,6}$ can be expressed as:

$$\text{Surface 3}: \iint_{S_3} U_x \left(0.5 U_y U_x + U_x' U_y'\right) \mathrm{d}S_3, \tag{7}$$

$$\text{Surface 4}: -\iint_{S_4} U_x \left(0.5 U_y U_x + U_x' U_y'\right) \mathrm{d}S_4, \tag{8}$$

$$\text{Surface 5}: -\iint_{S_5} U_x \left(0.5 U_z U_x + U_x' U_z'\right) \mathrm{d}S_5, \tag{9}$$

$$\text{Surface 6}: \iint_{S_6} U_x \left(0.5 U_z U_x + U_x' U_z'\right) \mathrm{d}S_6. \tag{10}$$

In this case, surfaces S_4 and S_5 are given negative signs such that flux entering and leaving the volume is denoted as positive and negative, respectively.

The advective and Reynolds stress contributions towards the fluxes through each surface, as denoted in Eq. (7), are presented in Figs. 18 and 19, respectively. The line-integrated fluxes across the denoted axial and lateral surfaces are computed as a function of the streamwise position x/D for the

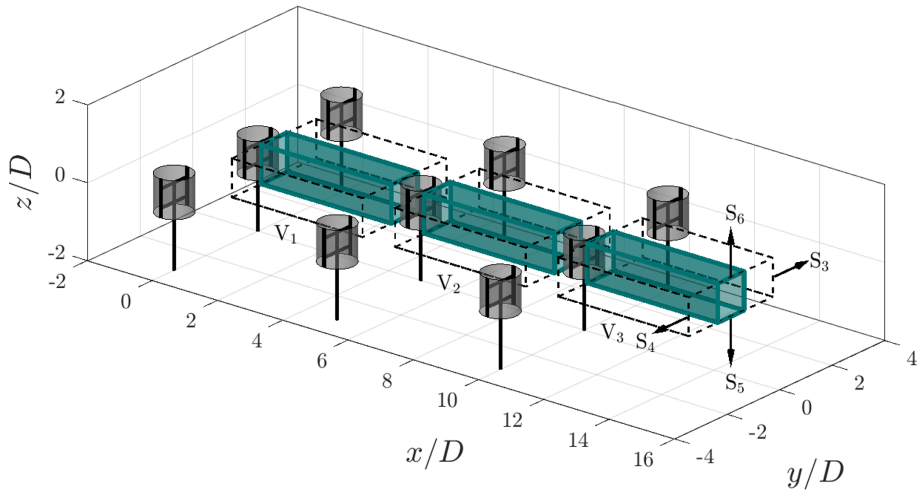

Figure 17. Schematic of the wind farm control volumes, denoted as V_1, V_2, and V_3, corresponding to the flow behind the first, second, and third rotor of the central column, respectively. The shaded regions are the volumes within the projected areas of the rotors of the central column ($-0.5 \leq y/D \leq 0.5$), while the dashed black lines indicate the edges of the central cells of the farm grid ($-1.6 \leq y/D \leq 1.6$). The fluxes are evaluated through the lateral and axial surfaces S_3, S_4, S_5, and S_6, respectively. The grey-shaded cylinders indicate the idealized AC surfaces of the rotors, which are shown at a phase-locked position of $\theta = 0°$.

three modes of operation within the farm grid lateral boundaries of $-0.5 \leq y/D \leq 0.5$. The values are normalized by $D/U_\infty^3 L$, where L is the integration length in the lateral direction; in this case, $L = D$.

For the baseline pitch case, a minimal flux across the lateral boundaries of the volume is visible, consistent with the flow field visualized in Sect. 4.3. The surfaces show a degree of symmetry consistent with the wake expansion shown in Sect. 4.3. For the negative pitch case, the trend in the flux on S_3 steadily decreases within a volume when travelling downstream, consistent with the lateral deflection of the wake core on the windward side of the rotor. Correspondingly, the flux on the leeward side of the rotor (S_4) is higher in magnitude, as high-momentum freestream flow is injected into the wake. This reaches increasing maximum magnitudes of 0.05, 0.06, and 0.08 in Volumes 1, 2, and 3, respectively. This increase in flux is apparent when considering Fig. 8, where an increasing asymmetric lateral inflow is shown as the CVP convects towards the upper and lower boundaries of the rotor. The positive pitch case exhibits the highest magnitude in lateral advection on S_3, reaching maximums of 0.07, 0.1, and 0.08 in Volumes 1, 2, and 3, respectively. This high lateral flux component is attributed to the ejection of the wake on the windward side of the rotor. Meanwhile, on S_4, there is an injection of momentum, which grows in magnitude between the first and second volumes. Leading up to the third rotor in the column, the momentum injection decreases significantly due to the wake of the neighbouring column on the leeward side.

Given the uniform inflow case of this study, the flow remains symmetric about the plane $z/D = 0$, as noted in the previous analysis in Sect. 4.3 and 4.2. Hence, the fluxes about S_5 and S_6 are also the same. Minor differences between the magnitudes of the two surfaces can be attributed to the tower's presence and other measurement noise. Hence, the discussion will focus on S_6 as the representative case. The positive pitch case shows the highest magnitudes in the first volume. The injection of momentum steadily decreases as the dominant CVP convects towards the windward direction. Compared to the baseline case, the flux steeply decreases leading up to the second rotor due to the upwind loaded induction. The baseline pitch case transitions from a positive flux as the wake expands to a negative value due to the asymmetric wake profile shown in Sect. 4.3, where flow is injected on the leeward side. This negative flux grows minimally in maximum magnitude between the volumes, from 0.02 to 0.03 in Volumes 1 and 3. Conversely, the negative pitch case shows a close-to-zero flux across the surface across all volumes. Although the wake is ejected out axially above the rotor, as shown in Sect. 4.3, the strong asymmetry in the wake and dominance of the lateral influx of momentum yield minimal vertical velocity magnitudes on the upper and lower surfaces of the rotor.

Overall, the fluxes of the Reynolds stress terms, illustrated in Fig. 19, are an order of magnitude lower than that of the advective, demonstrating the dominance of the advective terms over the Reynolds stresses in the recovery of kinetic energy in the farm. For all pitch cases, the highest magnitudes are concentrated near the wakes of the rotor. For the positive pitch, the largest magnitude flux is on S_3 due to the ejection of the wake. Unlike the case with the advective terms, the baseline case exhibits higher magnitudes in flux on the upper and lower surfaces of the control volume (S_5, S_6) compared to the pitched modes of operation. This highlights the relative importance of turbulent mixing towards the wake

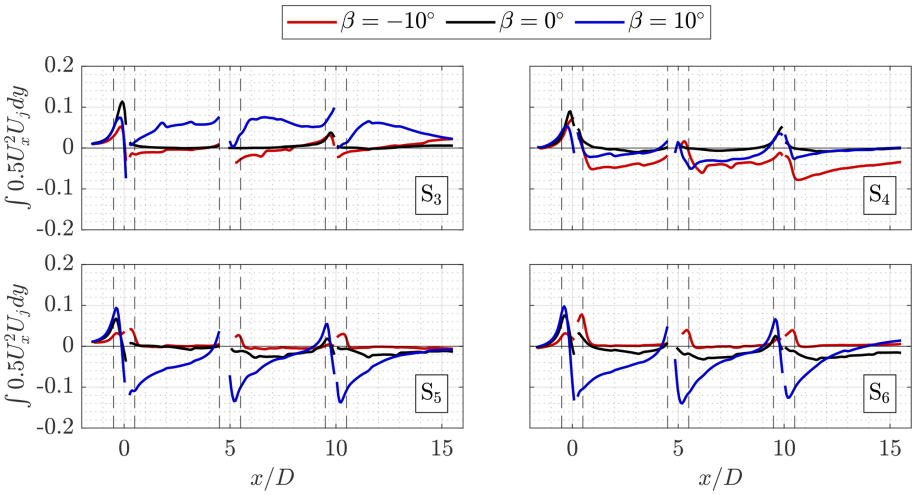

Figure 18. Line-integrated advective flux terms as a function of downstream position x/D through the surfaces $j = S_{3,4,5,6}$, as noted in Fig. 17 for the three modes of operation. The flux terms are integrated within the lateral boundaries $-0.5 \leq y/D \leq 0.5$. All values of fluxes are normalized by the ratio of the turbine diameter to the product of the freestream wind speed and lateral integration length, $1/U_\infty^3 L$, where $L = D$ in this case. The vertical dashed line denotes the edges of the central rotor volumes. The propagated relative errors following the spatially evolving uncertainties discussed in Sect. 3.5 are on the order of 1 %.

recovery for the baseline operation of the rotor. The spatial distributions of turbulent kinetic energy are presented in Appendix C.

The discussion above gives an indication of the surface fluxes as a function of the downstream location. The surface-integrated fluxes for each volume are shown in Fig. 20. Here, the sum of the advective and Reynolds stress contributions towards the flux is considered, as dictated in Eq. (7). In addition, the total flux of each surface over all three volumes is shown in the bottom tile of Fig. 20.

As discussed in relation to Fig. 18, the integrated fluxes of S_5 and S_6 remain similar due to symmetry for the three pitch cases. The negative pitch case shows a discrepancy in Volumes 2 and 3, with opposite signs of minimal magnitude. For the positive pitch case, the flux through S_3 decreases between Volumes 1 and 3 due to the presence of the wake of the neighbouring column. The vertical flux through S_6 also decreases in magnitude from 0.05 to 0.03 between Volumes 1 and 3. For the negative pitch case, the flux magnitude injection from S_4 increases from 0.04 to 0.06 between Volumes 1 and 3. In general, the largest fluxes for the baseline case are evident on the axial control surfaces, growing from 0.01 to 0.03 between Volumes 1 and 3, reaching a similar magnitude to the positive pitch case.

Considering the sums between all volumes for each control surface, it is evident that the positive pitch case exhibits the highest magnitude in flux, both with the ejection of the wake on S_3 and injection of high-momentum flow from S_6. The negative pitch case demonstrates the highest momentum injection through the leeward surface S_3. The baseline case demonstrates minimal flux across the lateral surfaces, with higher magnitudes in the vertical injection of momentum from S_6, attributed to the domain CVP discussed in Sect. 4.2.

To give a visual representation of the fluxes in the wind farm volume, the sum of the axial and lateral advective contributions towards the flux at discrete cross-stream planes $x/D = 2.5,\ 7.5,\ 12.5$ for the three modes of operation is shown in Fig. 21. The vectors show the in-plane velocity components, and the projected frontal area of the central rotor column and wind farm grid size are shown by solid and dashed lines, respectively. In this case, the magnitude of the in-plane velocity components is taken to compute the advective flux.

Consistent with Fig. 20, the positive pitch case demonstrates higher magnitudes in advective flux at all cross-stream locations. However, the largest magnitudes are present at the symmetry plane of the rotor $z/D = 0$, where the wake is ejected out laterally, driven by the dominant lateral flow component, as indicated by the vectors. This trend remains consistent on the windward side of the rotor. Meanwhile, on the leeward side, the wake of the neighbouring column connects within the measurement domain and projected frontal area of the rotor at $x/D = 12.5$, as evidenced in Fig. 10. However, as this wake has low magnitudes in streamwise flow, the advective transport of momentum is lower.

For the negative pitch case, larger magnitudes in advective momentum entrainment are present on the leeward side of the rotor, which grows in magnitude between the volume behind the first and second rotors in the column. This is consistent with the vortex topology discussed in Sect. 4.2.

Finally, for the baseline case, the advective flux is low behind the first rotor due to the lack of a dominant vortex pair in the wake, as shown in Sect. 4.2. Behind the second and

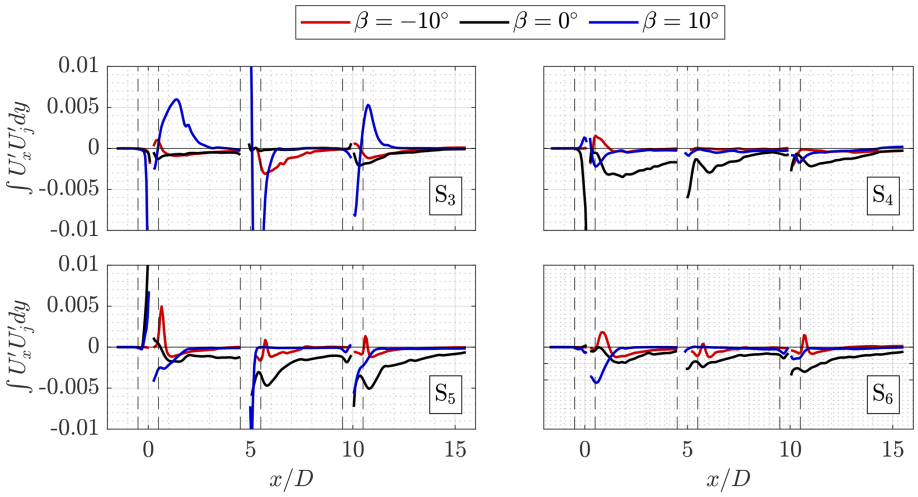

Figure 19. Line-integrated Reynolds stress flux terms as a function of downstream position x/D through the surfaces $j = S_{3,4,5,6}$, as noted in Fig. 17 for the three modes of operation. The flux terms are integrated within the lateral boundaries $-0.5 \leq y/D \leq 0.5$. All values of fluxes are normalized by the ratio of the turbine diameter to the product of the freestream wind speed and lateral integration length, $1/U_\infty^3 L$, where $L = D$ in this case. The vertical dashed line denotes the edges of the central rotor volumes.

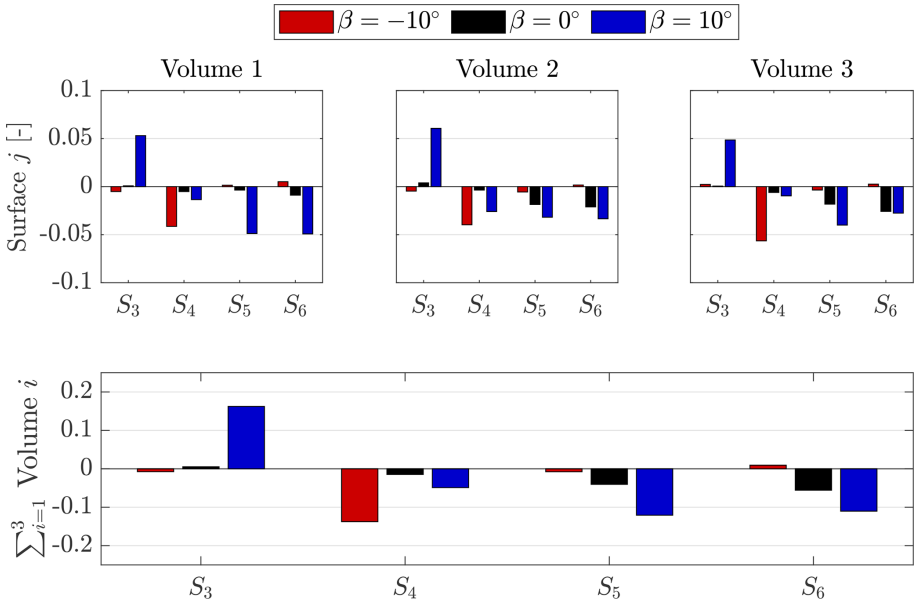

Figure 20. Surface integrals of the control surfaces ($j = 3, 4, 5$) as described in Eq. (7), where Volumes 1, 2, and 3 (i) correspond to the volumes behind the first, second, and third rotors, respectively. The sum of surface fluxes over all three volumes is shown in the bottom plot. All values are normalized by $1/U_\infty^3 S_i$. The surface areas between all four surfaces are constant, with $S_i = 4D^2$. The propagated relative error in the net volume flux following the spatially evolving uncertainties discussed in Sect. 3.5 is on the order of 1 %.

third rotors, advective flux is concentrated above and below the projected rotor surface, and the dominant cylinder-like vortex pair entrains momentum. However, the magnitude is not as high as the positive pitch case, as the streamwise flow components are lower in magnitude due to the wake incident on the first rotor in the column, as shown in Fig. 10.

To shed light on the total advective momentum flux within the farm grid area, the average sum of lateral and axial advective flux as a function of height z/D and cross-stream location x/D within the lateral domain $-1.6 \pm y/D \pm 1.6$ is shown in Fig. 22. Consistent with the results above, the positive pitch case demonstrates the highest magnitudes in advective flux, growing in size when progressing further downstream in the farm. High magnitudes of flux are concentrated around the top and bottom of the rotors as high-momentum flow is injected into the volume. Although the magnitudes

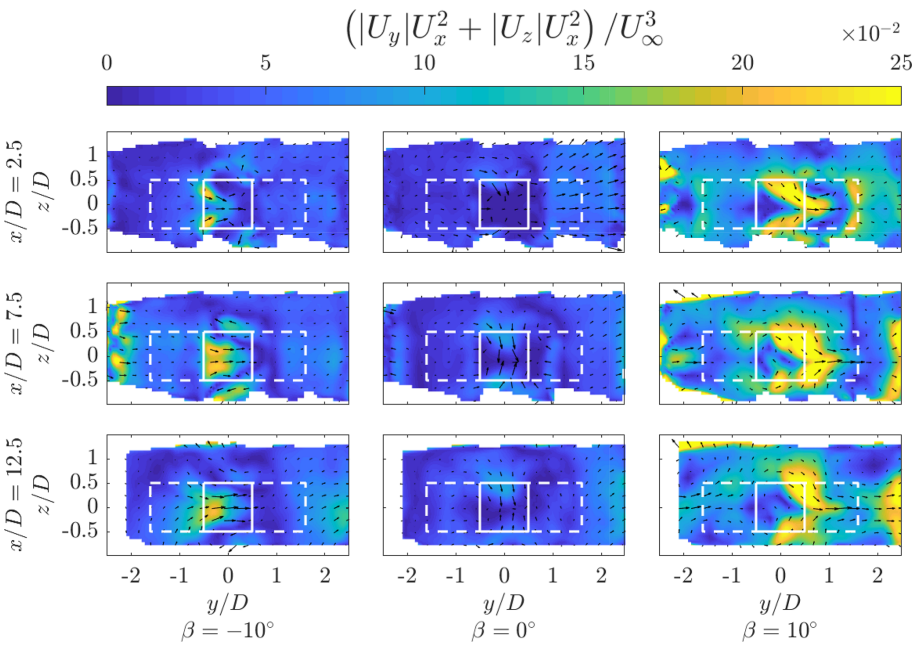

Figure 21. The sum of the lateral and axial advective contributions towards the flux at discrete cross-stream planes $x/D = 2.5$, 7.5, and 12.5 for the three pitch cases. The magnitudes of the velocity components $|U_y|$ and $|U_z|$ are considered to isolate the regions of momentum transfer. All values are normalized by the freestream velocity component U_∞^3. In-plane velocity vectors are also shown. The box delineated by the solid white line denotes the projected frontal area of the central rotor column, and the white dashed line denotes the grid size of the farm $-1.6 \leq y/D \leq 1.6$.

at mid-span are lower, they are still notable, as the wake is ejected outward laterally. The negative pitch case demonstrates minimal mean advective flux behind the first rotor but grows in magnitude to approximately 1.2 behind the second and third rotors. The shape confirms that most of the advection of flux occurs at the mid-span of the rotor. As expected, the baseline pitch case exhibits minimal magnitudes of flux, with no significant wake deflection. Marginally larger fluxes are apparent at the upper and lower surfaces of the rotor due to the dominant cylinder-like CVP commented on in Sect. 4.2.

5 Conclusions

This study provides the first experimental database of 3D-resolved time-averaged flow-field measurements for a wind-tunnel-scale high-energy-density wind farm made of VAWTs with and without wake control. The simulated farm consisted of nine rotors arranged in a grid fashion with fixed lateral and streamwise spacing of $3.18D$ and $5D$, respectively. In addition to the wake measurements for a baseline case, the wakes for two cases using the vortex generator wake control strategy, namely, with blade pitches of $\beta = -10°$ and $\beta = 10°$, were captured to highlight the re-generative wind farming capability of a VAWT farm.

The theory behind the vortex generator VAWT wake control strategy using a fixed blade pitch was described, highlighting the expected modes of re-energization in the wake for cases where the blades are pitched in versus pitched out. The modes of operation of the wake control strategy were confirmed by the streamwise vortex topology within the farm. An energization of the upwind and downwind vortices was achieved by pitching the blade inward and outward, respectively. For the former case, a significant influx of momentum from above and below the rotor was observed in the wake topology in parallel with a significant lateral deflection of the wake, consistent with thrust measurements of an isolated rotor. For the latter case, where the blades were pitched out, the downwind energized vortices induced an upwash of the wake while injecting high-momentum flow from the sides of the rotor.

The efficacy of these modes towards wake re-energization was highlighted by considering a proxy of the available power in the wake. The authors once again reiterate that, as the power of the rotors was not measured, the balance between the penalty associated with the steering turbine and that gained in the farm as a whole was not evaluated. The exaggerated pitch angles were selected to stay consistent with prior work performed by Huang (2023b) and to magnify the benefits associated with modifying the rotor loading with wake recovery in mind. However, such large pitch angles are likely not to be applied for full-scale rotors, especially positive pitches, given the unsteady load fluctuations stemming from the large degree of flow separation in the upwind pas-

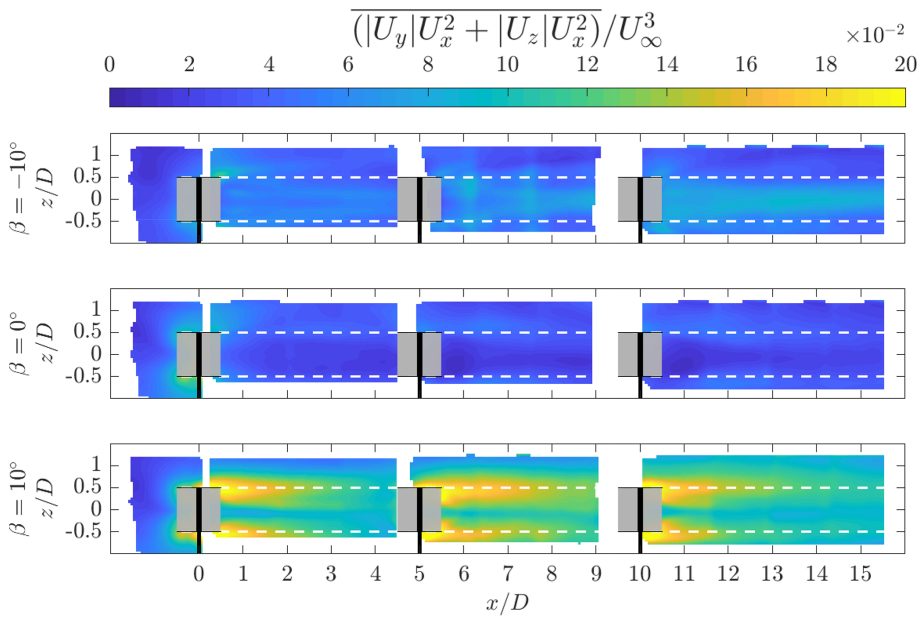

Figure 22. Average sum of the lateral and axial advective contributions towards the flux as a function of height z/D and cross-stream location x/D. The fluxes are averaged over the lateral domain $-1.6 \leq y/D \leq 1.6$ and normalized by the freestream flow U_∞^3. The grey-shaded region shows the rotors of the central column.

sage (Le Fouest and Mulleners, 2024). Nonetheless, these results demonstrate a proof-of-concept of the vortex generator mode for VAWT wake re-energization of a farm scale. When considering the case of a potential rotor directly in line with the central column, an available power recovery for the positive pitch case reaches a maximum of 72.4 % at $x/D = 3.2$, which is a factor of 6.4 higher than the baseline case. Meanwhile, the recovery within the farm for the negative pitch case reaches a maximum of 53 % at $x/D = 8.8$ (approx. $3D$ downstream of the second rotor), with a factor of 2.1 higher than the baseline case. This analysis was extended to allow for lateral offsets of hypothetical downstream rotors in the farm, highlighting the high potential for staggered arrangements. Although the positive pitch case showed the highest recovery rate for the inline rotor case, given the lateral deflection of the wake, the regions of high AP diminish on the windward side of the central column. These lucrative regions are further diminished on the farm when the wakes from the neighbouring columns begin to fall within the projected area of the rotor column. Finally, the re-energization mechanism of the farm was highlighted by adapting a volume analysis of the mean kinetic energy equation. The fluxes through the lateral and axial surfaces of the central rotor column confirm the working principle of the vortex generator mode and shed light on its efficacy on a farm scale.

The methodology and analysis presented can be extended in several directions, including the investigation of alternative turbine layouts (staggered vs. in-line) and the inclusion of a boundary layer, ground effect, and turbulent inflow. Furthermore, the database is valuable for the development and validation of numerical models in the context of "wind farming". This includes numerically validating the present results to evaluate the impacts of the neighbouring columns, tunnel blockage, and relevance towards an infinite farm wake topology. Future efforts should focus on quantifying the trade-offs between power loss in the steering turbine and the gain in the farm as a whole at a variety of operating conditions to yield more realistic passive and active pitch offsets. Meanwhile, structural metrics such as unsteady blade load and torque fluctuations should be considered, given their relevance to fatigue and turbine lifespan.

Appendix A: Sub-volume size

As discussed in Sect. 3.3, time-resolved particle tracks are spatially and temporally binned on a Cartesian grid. The impact of the selected sub-volume size (in voxels) and the resulting vector grid resolution Δx is presented in Fig. A1. In addition to the selected sub-volume size of 128 voxels used in this paper, the sizes of 52 voxels, 92 voxels, and 152 voxels are presented, with a 75 % overlap maintained for all cases. Normalized streamwise velocity U_x/U_∞ and turbulent kinetic energy (TKE) k/U_∞^2 profiles are presented, located at the symmetry plane $z/D = 0$ and at $x/D = 3.5$. Additionally, the root mean square of the differences of the quantities with respect to the 52 voxel case is presented, computed within the presented range of $-1.5 \leq y/D \leq 1.5$.

Overall, the selected sub-volume size has a minimal impact on the governing wake structure. Minor differences can be observed in the region of the maximum wake deficit,

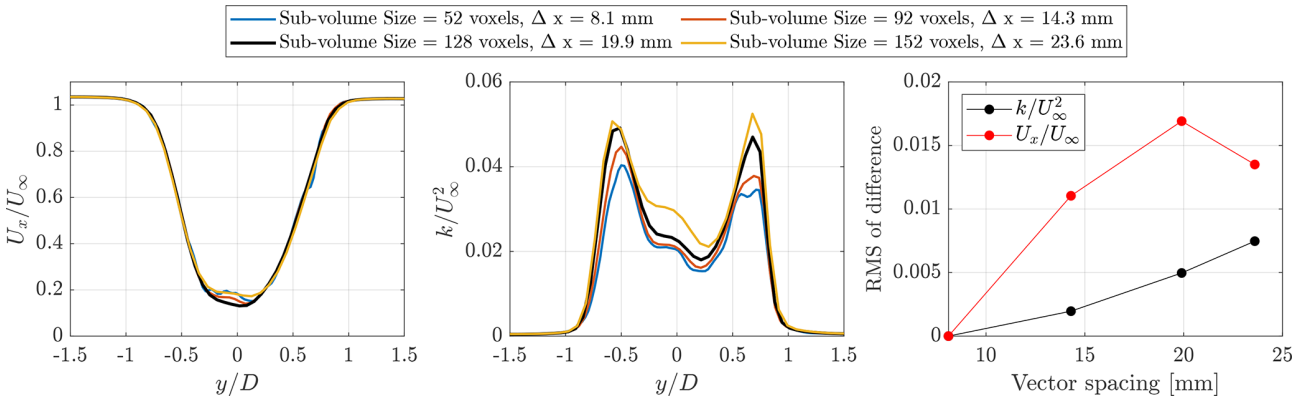

Figure A1. Profiles of the normalized streamwise velocity U_x/U_∞ and turbulent kinetic energy k/U_∞^2 along the symmetry plane $z/D = 0$ at the cross-stream location $x/D = 3.5$. The root mean square (RMS) of the difference with respect to the sub-volume size of 52 voxels is presented for both metrics.

likely due to a lack of convergence at the smallest sub-volume size. Meanwhile, the TKE shows a more noticeable difference, especially the most coarse resolution of 152 voxels. Larger sub-volume sizes will bin together regions with more discernible spatial and temporal fluctuations, mainly concentrated at the shear layer of the wake $y/D = \pm 0.5$. The root mean square of the differences at the selected sub-volume are $U_x/U_\infty = 1.7 \times 10^{-2}$ and $k/U_\infty^2 = 5.0 \times 10^{-3}$. Considering a representative value of $U_x/U_\infty = 0.2$ at the region of maximum difference, there is a relative error of 8.5 %. When considering a TKE of $k/U_\infty^2 = 0.05$ in the shear layer, the relative error is on the order of 10 %. The choice of a 128 voxel sub-volume with a grid size of $\Delta x = 19.9$ mm captures the governing wake shape while avoiding convergence issues at small sub-volumes. Given the minimal gains of resolving the turbulence along the shear layer and the relative importance of the advective contributions towards the wake recovery (discussed in Sect. 4.6), the benefits of a smaller sub-volume are outweighed by the required RAM, storage, and computation time, which are 15 times higher for the smallest sub-volume size.

Appendix B: Vorticity fields

As described in Sect. 2, the vortex generator mode of operation for VAWTs for wake control relies mainly on the modification of the streamwise vorticity ω_x, which has been thoroughly discussed in Sect. 4.2. Nonetheless, for completeness, the other vorticity components, namely, the axial ω_y and lateral ω_z, are shown in Figs. B1 and B2, respectively.

The lateral vorticity components ω_y for the baseline case $\beta = 0°$ show a strong symmetry between the upper and lower halves of the rotor with clockwise and anti-clockwise rotating structures, respectively. Such behaviour is also observed in the phase-locked measurements of Tescione et al. (2014) and field experiments of Wei et al. (2021). For the first rotor, the vortex structure transitions from an inboard movement

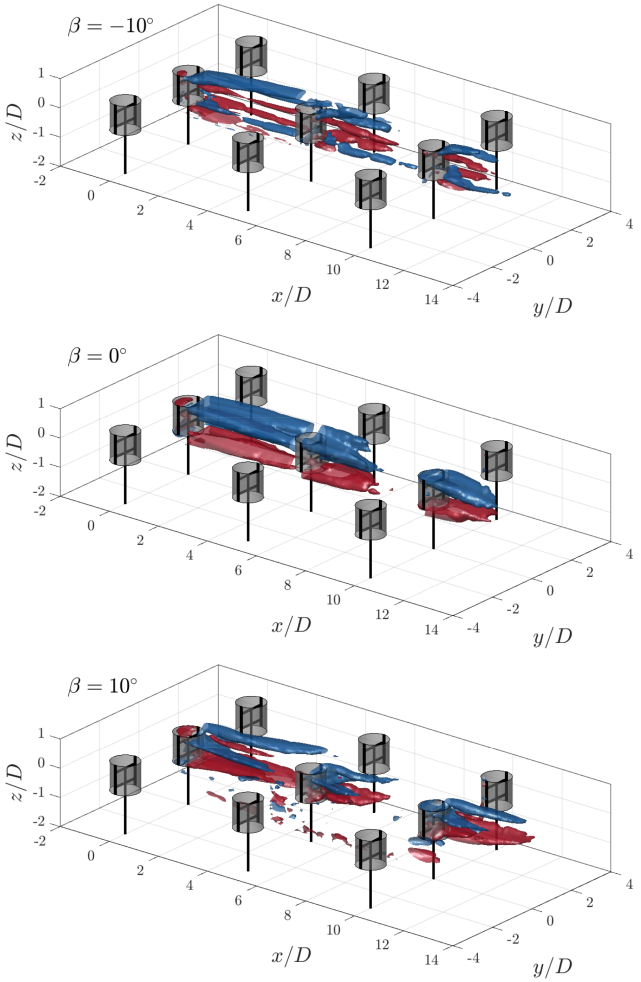

Figure B1. Iso-surfaces of the lateral vorticity contours at $\omega_y D/U_\infty = \pm 1$ for pitch cases $\beta = \pm 10°$ and $\beta = 0°$. The rotors are shown at a $\theta = 0°$ phase, with the grey-shaded cylinders representing the idealized actuator cylinder load.

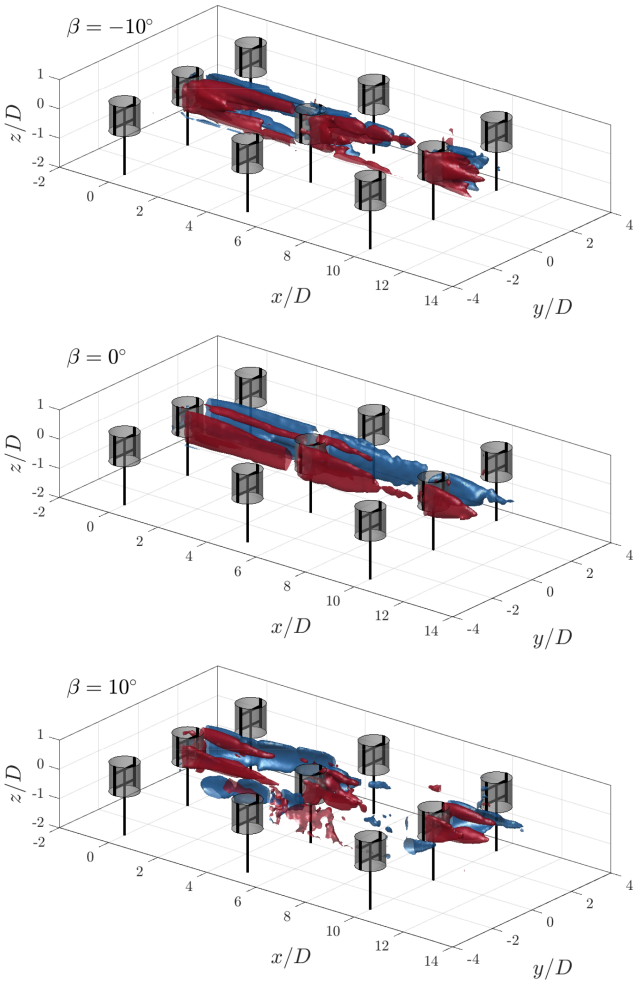

Figure B2. Iso-surfaces of the axial vorticity contours at $\omega_z D/U_\infty = \pm 1$ for pitch cases $\beta = \pm 10°$ and $\beta = 0°$. The rotors are shown at a $\theta = 0°$ phase, with the grey-shaded cylinders representing the idealized actuator cylinder load.

(towards $z/D = 0$) on the leeward half towards an outboard movement on the windward half. A similar trend was observed by Tescione et al. (2014). The subsequent rotors show a similar trend, with overall shortened vortex lengths due to the reduction in loads of the rotors. The vortex structure from the leeward side seems to extend further than those on the windward side, presumably a product of the reduction in load on the windward side due to the asymmetric wake of the first rotor, as discussed in Sect. 4.3.

For the positive pitch case $\beta = 10°$, the directions of the dominant vortices remain the same as in the baseline case. The structures deflect towards the windward side, consistent with the observations and discussion in Sect. 4.2.

The axial vorticity component ω_z is driven by the vortices shed along the span of the blades. For the baseline case, the dominant structure is clockwise and anti-clockwise on the windward and leeward sides, respectively. This is consistent with phase-locked measurements obtained by Tescione et al. (2014). As in the aforementioned case, the lengths of these structures are reduced for the subsequent rotors due to the reduction in load. On the windward side, the positive shear layer is also present, concentrated around the upper section of the rotor. This can be attributed to the asymmetric load and wake profile shown in Sect. 4.3, where a switch between the dominant contributor towards curl in the z direction $\mathrm{d}U_x/\mathrm{d}y$ would switch twice near the upper windward edge of the wake (given the mushroom-like shape). This would be asymmetric on the bottom half of the rotor but is absent due to the limited data on the bottom half of the rotor.

For the positive pitch case, the structures deflect laterally. Given the increase in the severity of the mushroom-like shape compared to the baseline case, the second positive shear layer on the windward side is also present and remains a feature for the subsequent rotors as well, with the asymmetric pair. Finally, for the negative pitch case, the shear layer on the windward side is deflected outwards, while that on the leeward side is contracted inward towards the core of the rotor, as flow is injected more heavily for the subsequent rotors in the farm.

Appendix C: Turbulent kinetic energy

As discussed in Sect. 4.6, the turbulent contributions towards the flux of mean kinetic energy within the projected volume of the central rotor column are several of orders magnitude lower than the advective contribution, in particular for the pitched cases. Turbulent inflow is of practical importance for wind farms, as it greatly influences rotor performance and blade fatigue, as commented on by Lee et al. (2012). The turbulent kinetic energy (TKE) at discrete cross-stream distances x/D = 2.5, 7.5, and 12.5 is shown in Fig. C1 for the three pitch cases.

Behind the first rotor, the distributions of TKE are qualitatively consistent with the measurements by Huang et al. (2023b) for an isolated rotor case of the same design, with the turbulence concentrated along the wake perimeter. As commented on by Huang et al. (2022), a longer wake perimeter is beneficial for facilitating momentum exchange due to turbulent diffusion along the shear layer. While the TKE remains concentrated within the projected frontal area of the baseline and negatively pitched case, it is ejected laterally outwards for the positive case, following the same trend discussed in Sect. 4.3. While this suggests a reduction in incoming turbulent flow for the rotors in the second row, it also shifts the source of turbulent contributions towards the streamwise momentum recovery away from the projected volume of the central column.

Behind the second and third rotors, the distributions of TKE contract in the axial directions for the baseline case, following the wake shape discussed in Sect. 4.3. While this suggests detrimental effects on the structural integrity of the

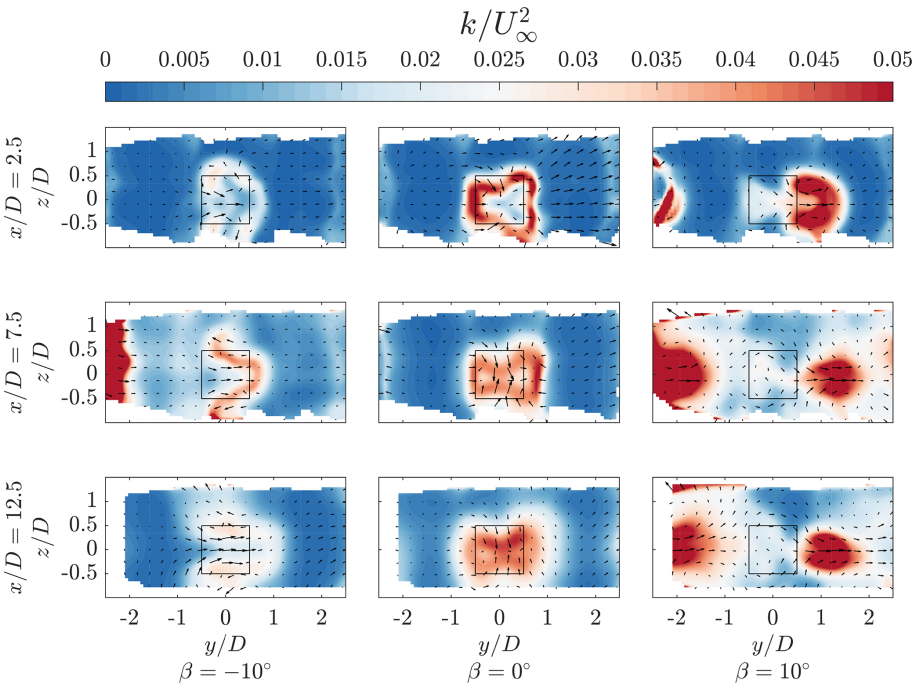

Figure C1. Normalized turbulent kinetic energy $k = \frac{1}{2}((U_x')^2 + (U_y')^2 + (U_z')^2)$ for the three pitch cases at streamwise locations $x/D = 2.5$, 7.5, and 12.5. The black-outlined square denotes the projected frontal area of the rotor, and the vectors show the in-plane velocity components.

subsequent rotors, the turbulent contributions towards the streamwise kinetic energy fluxes within the central rotor column would increase, consistent with the increases in magnitude of Reynolds stress fluxes on S_5 and S_6 behind the second and third rotors, as shown in Sect. 4.6. For the negative pitch case, the TKE remains concentrated along the laterally stretching wake on the windward side. Finally, for the positive pitch case, the concentration of TKE is absent within the projected frontal area of the central rotor column within the measurement domain, as the wakes are consistently deflected to the side. However, at $x/D = 7.5$ and $x/D = 12.5$, the regions of high TKE on the leeward side due to ejected wakes of the neighbouring column gradually enter the central volume.

Data availability. The data supporting this study's findings are openly available from 4TU ResearchData at https://doi.org/10.4121/7bf33a69-6542-41ee-af6d-3fd621b802e1.v1 (Bensason et al., 2025).

Author contributions. DB developed the methodology, carried out the experiment, performed the analysis, and wrote the paper. JM contributed towards the development of the methodology and carried out the experiment. AS revised the paper and provided scientific supervision during the experiment, analysis, and documentation phase. CF provided guidance towards the methodology, experiment, and analysis phase.

Competing interests. The contact author has declared that none of the authors has any competing interests.

Disclaimer. Publisher's note: Copernicus Publications remains neutral with regard to jurisdictional claims made in the text, published maps, institutional affiliations, or any other geographical representation in this paper. While Copernicus Publications makes every effort to include appropriate place names, the final responsibility lies with the authors.

Acknowledgements. We wish to thank the support of Ed Roessen and Rob van der List (Dienst Elektronische en Mechanische Ontwikkeling – AE Faculty) for the design and manufacturing of the rotors. Furthermore, thank you to Gert-Jan Berends (Aerodynamics Laboratory technician) for his critical role in the conceptualization and execution of the wind farm electronic systems. Finally, a special thank you to Delphine De Tavernier for her comprehensive review of the paper.

Financial support. This research was supported by the funding received from the European Union's Horizon 2020 research and innovation programme (grant no. 101007135) as part of the project XROTOR.

Review statement. This paper was edited by Sandrine Aubrun and reviewed by two anonymous referees.

References

Agüera, N., Cafiero, G., Astarita, T., and Discetti, S.: Ensemble 3D PTV for high resolution turbulent statistics, Meas. Sci. Technol., 27, 124011, https://doi.org/10.1088/0957-0233/27/12/124011, 2016.

Bachant, P. and Wosnik, M.: Effects of Reynolds number on the energy conversion and near-wake dynamics of a high solidity vertical-axis cross-flow turbine, Energies, 9, 73, https://doi.org/10.3390/en9020073, 2016.

Barthelmie, R. J., Frandsen, S. T., Nielsen, M., Pryor, S., Rethore, P.-E., and Jørgensen, H. E.: Modelling and measurements of power losses and turbulence intensity in wind turbine wakes at Middelgrunden offshore wind farm, Wind Energy, 10, 517–528, 2007.

Barthelmie, R. J., Pryor, S. C., Frandsen, S. T., Hansen, K. S., Schepers, J., Rados, K., Schlez, W., Neubert, A., Jensen, L., and Neckelmann, S.: Quantifying the impact of wind turbine wakes on power output at offshore wind farms, J. Atmos. Ocean. Tech., 27, 1302–1317, 2010.

Bastankhah, M. and Porté-Agel, F.: Experimental and theoretical study of wind turbine wakes in yawed conditions, J. Fluid Mech., 806, 506–541, 2016.

Bensason, D., Simley, E., Roberts, O., Fleming, P., Debnath, M., King, J., Bay, C., and Mudafort, R.: Evaluation of the potential for wake steering for U.S. land-based wind power plants, J. Renew. Sustain. Energ., 13, 033303, https://doi.org/10.1063/5.0039325, 2021.

Bensason, D., Sciacchitano, A., and Ferreira, C.: Near wake of the X-Rotor vertical-axis wind turbine, J. Phys. Conf. Ser., 2505, 012040, https://doi.org/10.1088/1742-6596/2505/1/012040, 2023.

Bensason, D., Sciacchitano, A., Giri Ajay, A., and Simao Ferreira, C.: A Study of the Near Wake Deformation of the X-Rotor Vertical-Axis Wind Turbine With Pitched Blades, Wind Energy, 27, 1388–1411, 2024.

Bensason, D., Mulay, J., Sciacchitano, A., and Simao Ferreira, C.: Supporting data belonging to publication: "Experimental demonstration of regenerative wind farming using a high-density layout of VAWTs", Version 1, 4TU.ResearchData [data set], https://doi.org/10.4121/7bf33a69-6542-41ee-af6d-3fd621b802e1.v1, 2025.

Bossuyt, J., Scott, R., Ali, N., and Cal, R. B.: Quantification of wake shape modulation and deflection for tilt and yaw misaligned wind turbines, J. Fluid Mech., 917, A3, https://doi.org/10.1017/jfm.2021.237, 2021.

Boudreau, M. and Dumas, G.: Comparison of the wake recovery of the axial-flow and cross-flow turbine concepts, J. Wind Eng. Ind. Aerod., 165, 137–152, 2017.

Brownstein, I. D., Wei, N. J., and Dabiri, J. O.: Aerodynamically interacting vertical-axis wind turbines: Performance enhancement and three-dimensional flow, Energies, 12, 2724, https://doi.org/10.3390/en12142724, 2019.

Caridi, G. C. A., Ragni, D., Sciacchitano, A., and Scarano, F.: HFSB-seeding for large-scale tomographic PIV in wind tunnels, Exp. Fluids, 57, 1–13, 2016.

Cortina, G., Calaf, M., and Cal, R. B.: Distribution of mean kinetic energy around an isolated wind turbine and a characteristic wind turbine of a very large wind farm, Phys. Rev. Fluids, 1, 074402, https://doi.org/10.1103/PhysRevFluids.1.074402, 2016.

Cossu, C.: Evaluation of tilt control for wind-turbine arrays in the atmospheric boundary layer, Wind Energ. Sci., 6, 663–675, https://doi.org/10.5194/wes-6-663-2021, 2021.

Dabiri, J. O.: Potential order-of-magnitude enhancement of wind farm power density via counter-rotating vertical-axis wind turbine arrays, J. Renew. Sustain. Energ., 3, 043104, https://doi.org/10.1063/1.3608170, 2011.

De Tavernier, D. and Ferreira, C.: An extended actuator cylinder model: actuator-in-actuator cylinder (AC-squared) model, Wind Energy, 22, 1058–1070, 2019.

De Tavernier, D., Ferreira, C., Li, A., Paulsen, U., and Madsen, H.: Towards the understanding of vertical-axis wind turbines in double-rotor configuration, J. Phys. Conf. Ser., 1037, 022015, https://doi.org/10.1088/1742-6596/1037/2/022015, 2018.

De Tavernier, D., Ferreira, C., Paulsen, U., and Madsen, H.: The 3D effects of a vertical-axis wind turbine: rotor and wake induction, J. Phys. Conf. Ser., 1618, 052040, https://doi.org/10.1088/1742-6596/1618/5/052040, 2020.

Faleiros, D. E., Tuinstra, M., Sciacchitano, A., and Scarano, F.: Generation and control of helium-filled soap bubbles for PIV, Exp. Fluids, 60, 1–17, 2019.

Fleming, P., Annoni, J., Shah, J. J., Wang, L., Ananthan, S., Zhang, Z., Hutchings, K., Wang, P., Chen, W., and Chen, L.: Field test of wake steering at an offshore wind farm, Wind Energ. Sci., 2, 229–239, https://doi.org/10.5194/wes-2-229-2017, 2017.

Fleming, P., King, J., Simley, E., Roadman, J., Scholbrock, A., Murphy, P., Lundquist, J. K., Moriarty, P., Fleming, K., van Dam, J., Bay, C., Mudafort, R., Jager, D., Skopek, J., Scott, M., Ryan, B., Guernsey, C., and Brake, D.: Continued results from a field campaign of wake steering applied at a commercial wind farm – Part 2, Wind Energ. Sci., 5, 945–958, https://doi.org/10.5194/wes-5-945-2020, 2020.

Giaquinta, D.: The Flow Topology of the Ahmed Body in Cross-Wind, Ph.D. thesis, MSc Thesis. Delft University of Technology, Department of Aerospace Engineering, https://doi.org/10.18726/2019_3, 2018.

Guo, J. and Lei, L.: Flow characteristics of a straight-bladed vertical axis wind turbine with inclined pitch axes, Energies, 13, 6281, https://doi.org/10.3390/en13236281, 2020.

Hezaveh, S. H. and Bou-Zeid, E.: Mean kinetic energy replenishment mechanisms in vertical-axis wind turbine farms, Phys. Rev. Fluids, 3, 094606, https://doi.org/10.1103/PhysRevFluids.3.094606, 2018a.

Hezaveh, S. H., Bou-Zeid, E., Dabiri, J., Kinzel, M., Cortina, G., and Martinelli, L.: Increasing the power production of vertical-axis wind-turbine farms using synergistic clustering, Bound.-Lay. Meteorol., 169, 275–296, 2018b.

Howland, M. F., Bossuyt, J., Martínez-Tossas, L. A., Meyers, J., and Meneveau, C.: Wake structure in actuator disk models of wind turbines in yaw under uniform inflow conditions, J. Renew. Sustain. Energ., 8, 043301, https://doi.org/10.1063/1.4955091, 2016.

Howland, M. F., Lele, S. K., and Dabiri, J. O.: Wind farm power optimization through wake steering, P. Natl. Acad. Sci. USA, 116, 14495–14500, 2019.

Huang, M.: Wake and wind farm aerodynamics of vertical axis wind turbines, Ph.D. thesis, ISBN 9789055841745,

https://doi.org/10.4233/uuid:14619578-e44f-45bb-a213-a9d179a54264, 2023b.

Huang, M., Ferreira, C., Sciacchitano, A., and Scarano, F.: Wake scaling of actuator discs in different aspect ratios, Renew. Energ., 183, 866–876, 2022.

Huang, M., Sciacchitano, A., and Ferreira, C.: Experimental and numerical study of the wake deflections of scaled vertical axis wind turbine models, J. Phys. Conf. Ser., 2505, 012019, https://doi.org/10.1088/1742-6596/2505/1/012019, 2023a.

Huang, M., Sciacchitano, A., and Ferreira, C.: On the wake deflection of vertical axis wind turbines by pitched blades, Wind Energy, 26, 365–387, https://doi.org/10.1002/we.2803, 2023b.

Huang, M., Vijaykumar Patil, Y., Sciacchitano, A., and Ferreira, C.: Experimental study of the wake interaction between two vertical axis wind turbines, Wind Energy, 26, 1188–1211, https://doi.org/10.1002/we.2863, 2023c.

Kasper, J. H. and Stevens, R. J.: Effects of wind turbine rotor tilt on large-scale wind farms, J. Phys. Conf. Ser., 2767, 092072, https://doi.org/10.1088/1742-6596/2767/9/092072, 2024.

Le Fouest, S. and Mulleners, K.: Optimal blade pitch control for enhanced vertical-axis wind turbine performance, Nat. Commun., 15, 2770, https://doi.org/10.1038/s41467-024-46988-0, 2024.

LeBlanc, B. and Ferreira, C.: Estimation of blade loads for a variable pitch vertical axis wind turbine from particle image velocimetry, Wind Energy, 25, 313–332, https://doi.org/10.1002/we.2674, 2022a.

LeBlanc, B. and Ferreira, C.: Estimation of blade loads for a variable pitch Vertical Axis Wind Turbine with strain gage measurements, Wind Energy, 25, 1030–1045, https://doi.org/10.1002/we.2713, 2022b.

Lee, S., Churchfield, M., Moriarty, P., Jonkman, J., and Michalakes, J.: Atmospheric and wake turbulence impacts on wind turbine fatigue loadings, in: 50th AIAA Aerospace Sciences Meeting including the New Horizons Forum and Aerospace Exposition, 9–12 January, 2012, Nashville, Tennessee, p. 540, 2012.

Lignarolo, L., Ragni, D., Krishnaswami, C., Chen, Q., Ferreira, C. S., and Van Bussel, G.: Experimental analysis of the wake of a horizontal-axis wind-turbine model, Renew. Energy, 70, 31–46, 2014.

Lignarolo, L., Ragni, D., Scarano, F., Ferreira, C. S., and Van Bussel, G.: Tip-vortex instability and turbulent mixing in wind-turbine wakes, J. Fluid Mech., 781, 467–493, 2015.

Madsen, H. A., Paulsen, U. S., and Vitae, L.: Analysis of VAWT aerodynamics and design using the Actuator Cylinder flow model, J. Phys. Conf. Ser., 555, 012065, https://doi.org/10.1088/1742-6596/555/1/012065, 2014.

Martinez-Ojeda, E., Solorio Ordaz, F. J., and Sen, M.: Vertical-axis wind-turbine computations using a 2D hybrid wake actuator-cylinder model, Wind Energ. Sci., 6, 1061–1077, https://doi.org/10.5194/wes-6-1061-2021, 2021.

Mendoza, V. and Goude, A.: Improving farm efficiency of interacting vertical-axis wind turbines through wake deflection using pitched struts, Wind Energy, 22, 538–546, 2019.

Möller, B., Hong, L., Lonsing, R., and Hvelplund, F.: Evaluation of offshore wind resources by scale of development, Energy, 48, 314–322, 2012.

Porté-Agel, F., Bastankhah, M., and Shamsoddin, S.: Wind-turbine and wind-farm flows: a review, Bound.-Lay. Meteorol., 174, 1–59, 2020.

Raffel, M., Willert, C. E., Scarano, F., Kähler, C. J., Wereley, S. T., and Kompenhans, J.: Particle image velocimetry: a practical guide, Springer, https://doi.org/10.1007/978-3-319-68852-7, 2018.

Ribeiro, A. F., Ferreira, C. S., and Casalino, D.: Vertical axis wind turbine wake steering by pitched struts and blades, J. Phys. Conf. Ser., 2767, 092004, https://doi.org/10.1088/1742-6596/2767/9/092004, 2024.

Rolin, V. F. and Porté-Agel, F.: Experimental investigation of vertical-axis wind-turbine wakes in boundary layer flow, Renew. Energy, 118, 1–13, 2018.

Ryan, K. J., Coletti, F., Elkins, C. J., Dabiri, J. O., and Eaton, J. K.: Three-dimensional flow field around and downstream of a subscale model rotating vertical axis wind turbine, Exp. Fluids, 57, 1–15, 2016.

Scarano, F.: Tomographic PIV: principles and practice, Measurement Science and Technology, 24, 012001, https://doi.org/10.1088/0957-0233/24/1/012001, 2012.

Schanz, D., Gesemann, S., and Schröder, A.: Shake-The-Box: Lagrangian particle tracking at high particle image densities, Exp. Fluids, 57, 1–27, 2016.

Schneiders, J. F., Caridi, G. C., Sciacchitano, A., and Scarano, F.: Large-scale volumetric pressure from tomographic PTV with HFSB tracers, Exp. Fluids, 57, 1–8, 2016.

Shaler, K., Jonkman, J., Barter, G. E., Kreeft, J. J., and Muller, J. P.: Loads assessment of a fixed-bottom offshore wind farm with wake steering, Wind Energy, 25, 1530–1554, 2022.

Shields, M., Beiter, P., Nunemaker, J., Cooperman, A., and Duffy, P.: Impacts of turbine and plant upsizing on the levelized cost of energy for offshore wind, Appl. Energ., 298, 117–189, https://doi.org/10.1016/j.apenergy.2021.117189, 2021.

Sørensen, J. N.: Instability of helical tip vortices in rotor wakes, J. Fluid Mech., 682, 1–4, 2011.

Sørensen, J. N. and Larsen, G. C.: A minimalistic prediction model to determine energy production and costs of offshore wind farms, Energies, 14, 448, https://doi.org/10.3390/en14020448, 2021.

Stevens, R. J. and Meneveau, C.: Flow structure and turbulence in wind farms, Annu. Rev. Fluid Mech., 49, 311–339, 2017.

Tescione, G., Ragni, D., He, C., Ferreira, C. S., and Van Bussel, G.: Near wake flow analysis of a vertical axis wind turbine by stereoscopic particle image velocimetry, Renew. Energy, 70, 47–61, 2014.

van der Hoek, D., den Abbeele, B. V., Simao Ferreira, C., and van Wingerden, J.-W.: Maximizing wind farm power output with the helix approach: Experimental validation and wake analysis using tomographic particle image velocimetry, Wind Energy, 27, 463–482, https://doi.org/10.1002/we.2896, 2024.

Vergaerde, A., De Troyer, T., Muggiasca, S., Bayati, I., Belloli, M., Kluczewska-Bordier, J., Parneix, N., Silvert, F., and Runacres, M. C.: Experimental characterisation of the wake behind paired vertical-axis wind turbines, J. Wind Eng. Ind. Aerod., 206, 104 353, https://doi.org/10.1016/j.jweia.2020.104353, 2020.

Wei, N. J., Brownstein, I. D., Cardona, J. L., Howland, M. F., and Dabiri, J. O.: Near-wake structure of full-scale vertical-axis wind turbines, J. Fluid Mech., 914, A17, https://doi.org/10.1017/jfm.2020.578, 2021.

Wieneke, B.: Volume self-calibration for 3D particle image velocimetry, Exp. Fluids, 45, 549–556, 2008.